PONTIFICAL CATHOLIC UNIVERSITY OF CHILE

FACULTY OF PHYSICS

PHYSICS INSTITUTE

COSMIC RAY TESTS FOR THE QS1 MODULE OF THE NEW SMALL WHEEL IN THE ATLAS EXPERIMENT

—AND—

PROSPECTS ON THE SEARCH FOR HEAVY VECTOR TRIPLET BOSONS IN THE LEPTONIC DECAY CHANNELS WITH THE ATLAS EXPERIMENT AT THE HL-LHC

BY

JUAN CRISTÓBAL RIVERA VERGARA

Masters thesis presented to the Physics
Institute of the Pontifical Catholic University of Chile,
to opt to the degree of Master in Physics.

Supervising Professor	:	PhD. Juan Pedro Ochoa-Ricoux
Comission	:	PhD. Marco Aurelio Díaz
		PhD. Benjamin Koch

November, 2018

Santiago, Chile

Acknowlegdments

I would like to thank my Family, specially my mom and dad, for supporting and encouraging me in this carreer choice.

I would like to thank my advisor and mentor Juan Pedro Ochoa-Ricoux for his teachings and his patience. I would also like to thank the ATLAS hardware team and the ATLAS analysis team: Graham Lee, Sebastián Olivares, Roberto Pinto, Juan Pablo Moraga, Juan Pablo Elorrieta and Professors Marco Aurelio Díaz and Ángel Abusleme for all their help and advice.

I would like to thank my friends, for helping me relax, enjoy myself and have some fun when things get too hard.

And specially, I would like to thank my girlfriend Carmen Stappung, for her love, her jokes, her smiles, for putting up with all my physics speeches, and for being there whenever I needed someone.

Abstract

The ATLAS detector at the LHC, CERN, will be upgraded after the current data taking period (Run 2). The ATLAS detector has to undergo a series of upgrades in order to fulfill the needed performance at improved LHC conditions. The LHC will stop for the second time between 2019-2020, period of time during which the ATLAS detector is going to upgrade its muon subdetector. This upgrade is the New Small Wheel (NSW), which will replace part of its endcap muon spectrometer. The NSW will be comprised of two detection systems, the MicroMegas and the small-strip Thin Gap Chambers (sTGC), the latest is being constructed in Chile by a joint collaboration between PUC and UTFSM. After the construction, the chambers are tested before being shipped to CERN. The muon detection efficiency is calculated using cosmic muons. A trigger system is used as part of the setup, which checks for coincidences between plastic scintillator arrays placed on top and below the detectors in order to distinguish muons from background signals. A DAQ system is used to callibrate the electronics and measure muon hits. The whole system has been set up and has already been used to test one module that was successfully sent to CERN and integrated into the first wedge.

Prospects were made for searches for new heavy SSM Z' and W' bosons at the last stage of the LHC (2024-2032), called High Luminosity LHC (HL-LHC), which is expected to run at $\sqrt{s} = 14$ TeV and collect 3000 fb^{-1} of data. These studies are based on MC simulations, and are used as benchmark for other models. The response of the upgraded ATLAS detector as well as pile-up

collisions were simulated. SSM Z' bosons are searched for in the dilepton final states, where it is expected to observe a signal with a more than five significance value at an invariant mass of 6.4 TeV, and exclude masses up to 6.5 TeV. SSM W' bosons are searched for in the lepton plus neutrino final state, where it is expected to observe a signal with a more than five significance value at an invariant mass of 7.7 TeV, and exclude masses up to 7.9 TeV.

Contents

List of Figures

Part I

Introduction and Basics

Chapter 1

Introduction

The Pontifical Catholic University of Chile (PUC) has a dedicated ATLAS hardware team, which in turn is part of an ATLAS upgrade project: the New Small Wheel (NSW). The NSW is to be installed at the ATLAS detector during the Long Shutdown 2, after Run 2 (2019-2020), and the construction of the different components of the upgrade are completed at various sites around the world: Canada, China, Israel, Russia and Chile. In Chile the tasks are separated further between two institutions: the Technical University Federico Santa María (UTFSM), and PUC. The UTFSM is in charge of the main construction, and the PUC is in charge of the final steps of the construction, and the Quality Assurance (QA) tests.

Part of the work that has to be conducted are the cosmic ray tests for the NSW, as part of the QA tests that are to be done on the modules produced in Chile. These tests are meant to measure the efficiencies, resolutions, and noise levels, among other things, of the different parts of the modules. As a bonus, it allows finding any issues that might have arisen during the construction. In order to be able to process the data efficiently, it is necessary to provide the module with a trigger signal to control the measurements. To trigger the module plastic scintillators are used, which can be used to detect cosmic ray muons. By having a scintillator on top of the module and another one below it, coincidences in the signals can be checked. This is used as confirmation that a muon has passed through both of them, and consequently, through the module. The data from that measured muon can be used to determine the different values that we are trying to measure.

Alongside the hardware team, there is also an ATLAS analysis team at PUC, part of which works on the prospects for a search for SSM Z' and W' bosons, using the upgraded ATLAS detector for the HL-LHC. This work has as its main goal to evaluate the impact that the upgrades of ATLAS, as well as the increase in Luminosity, will have on the limits that can be set on possible future measurements.

For this, simulated data is used, which takes into consideration the expected changes to the detector, as well as the increase in statistics. This allows the use of different values for the expected efficiencies, as well as integrated luminosities, and gauging the impact of these changes. Also the results can be compared with the previous results that were obtained using real data, which allows to see by how much the exclusion and discovery limits of such searches are affected by the detector upgrades that are planned.

Thus, this thesis will be divided into two main sections: the first will be about the work done on the Cosmic Ray Tests for the NSW, while the second one will focus on the analysis work on the search prospects for SSM Z' and W' bosons using the upgraded ATLAS detector at the HL-LHC.

Chapter 2

The Large Hadron Collider at CERN

2.1 Physics Motivation

The Standard Model (SM) of particle physics is the theory that describes three of the four known fundamental forces of the universe (electromagnetic, weak, and strong interactions, doesn't include gravity), and also classifies the known fundamental particles. It has successfully predicted many experimental observations, yet it still leaves a few phenomena unexplained, and is thus not considered a complete theory. However, given its accuracy, it is often taken as a basis for new models that seek to explain the gaps that the SM leaves unanswered.

Phenomena such as dark matter, neutrino oscillations, baryon asymmetry, the accelerating expansion of the universe, and even gravity, are not fully explained by the SM, and so new theories explaining these phenomena have to be formulated and tested. Physicists do this by trying to measure the differences in the predictions between the new models and the SM.

Besides trying to measure new particles, physicists also try to improve the precision of the measurements that have already been done. There are also a number of parameters that are not given by the theory and that have to be measured directly. These often require very precise measurements, with large statistics.

In order to do all of these, large experiments are conducted, usually by multinational collaborations. For example the LHC in CERN (both explained below), is able to accelerate particles to speeds very close to the speed of light, granting them energies close to the ones they had seconds after the Big Bang. The particles are collided in various points, where new particles are produced as a result of these collisions. There, physicists have built detectors designed specifically to study these new particles, as well as measure their properties. The data is later analyzed, and with it new discoveries can be made.

One example of this would be the discovery of the Higgs boson, which was predicted by the SM. In 2013 physicists were able to finally measure the production of a Higgs-like particle in various decay channels. Figure 2.1 shows one of the decay channels used in the analysis. This plot corresponds to the one obtained using the data produced at ATLAS, one of the experiments at the LHC in CERN. This experiment is the focus of the following chapter.

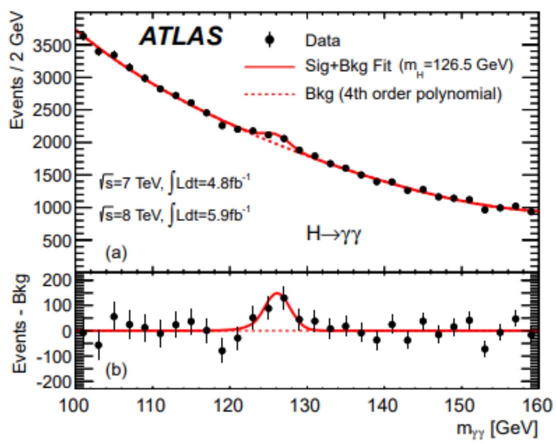

Figure 2.1: Invariant $\gamma\gamma$ mass plot. [1]

2.2 CERN

CERN (from the french: *Conseil européen pour la recherche nucléaire*) is a European research organization that operates the largest particle physics experiments in the world. Established in 1954, it has been the home of various High Energy Physics experiments, housed at various Particle Accelerators, such the Super Proton Synchrotron (SPS) and the Large Electron Positron Collider (LEP). Several scientific achievements have been made at CERN, such as the discovery of the Z and W bosons, the discovery of the Higgs boson, among others. The latter was made possible thanks to the Large Hadron Collider (LHC), the largest particle collider to date.

2.3 The Large Hadron Collider

The LHC is the largest and most powerful particle collider in the world. It uses a set of increasingly large ring shaped magnets to accelerate protons to speeds close to the speed of light (see figure 2.2). Each ring accelerates the protons to a certain nominal speed, before feeding them into the next ring in the sequence, which will accelerate the particles even further. Right before reaching the main ring, the protons are separated into two beams, going in opposite directions as they enter the final LHC ring, which is 27 km in circumference. After being accelerated to the desired speeds, the proton beams collide at four crossing points with energies up to 13 TeV, and the resulting debris is detected by 7 detectors: ATLAS, CMS, LHCb, ALICE, TOTEM, LHCf, and MoEDAL. This allows physicists to observe new particles that are unobservable in nature.

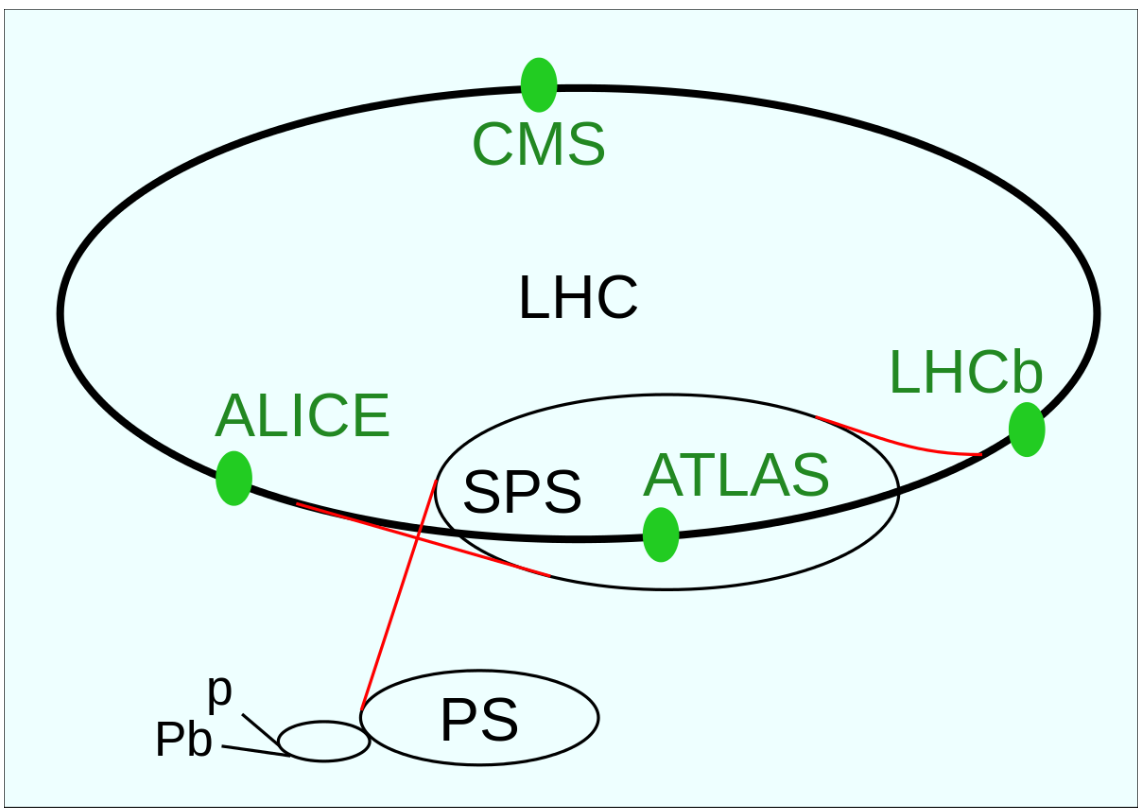

Figure 2.2: Rings that form the LHC. Protons (or sometimes lead nuclei) are injected into the Proton Synchrotron (PS), which accelerates them and injects them into the Super Proton Synchrotron (SPS), which accelerates them even higher and later injects two beams into the largest LHC ring. Four of the seven experiments are highlighted in the diagram. [2]

Chapter 3

The ATLAS Experiment

At one of the beam crossing points is ATLAS (A Toroidal LHC ApparatuS), a multipurpose detector that is able to reconstruct the trajectory, energy and momenta of the particles produced in the collisions with high precision and efficiency. In order to do that, it uses many different types of detectors, each designed to detect specific types of particles. The main sections are: the Inner Tracker, the Calorimeters, the Magnet System, and the Muon Spectrometer. Figure 3.1 shows the ATLAS detector, with some of its many sub-components. ATLAS is also subdivided into 3 areas: the barrel, which consists of all the detectors that align parallel to the beam, the endcaps, which are the parts that are perpendicular to the beam and are located at both ends of ATLAS, and finally the forward region, contained within the endcaps, but much closer to the beam.

A common coordinate system is used throughout ATLAS. The interaction point is defined as the origin of the coordinate system. The z-axis runs along the beam line. The x-y plane is perpendicular to the beam line and is referred to as the transverse plane. The positive x-axis points from the interaction point to the center of the LHC ring; the positive y-axis points upward to the surface of the earth. The transverse plane is often described in terms of r-ϕ coordinates. The azimuthal angle ϕ is measured from the x-axis, around the beam. The radial dimension, r, measures the distance from the beam line. The polar angle θ is defined as the angle from the positive z-axis. The polar angle is often reported in terms of pseudorapidity, defined as:

$$\eta \equiv -\ln\left[\tan\left(\frac{\theta}{2}\right)\right] \tag{3.1}$$

This means, that for θ perpendicular to the beam, i.e. pointing along the transverse plane, $\eta = 0$, and for θ going to 0, or getting closer to the beam line, η goes to infinity. The distance ΔR is defined in η-ϕ space as:

$$\Delta R = \sqrt{\Delta\eta^2 + \Delta\phi^2} \tag{3.2}$$

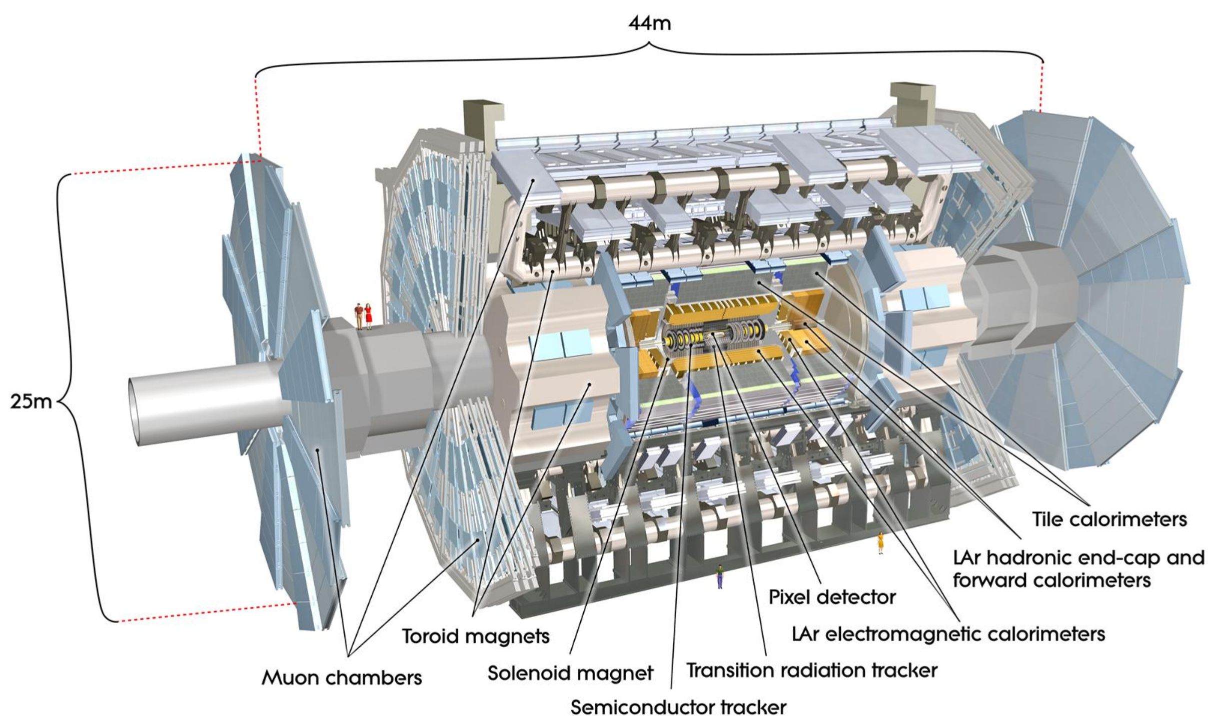

Figure 3.1: The ATLAS Detector. Various parts of it are indicated, which will be explained in the sections below. [3]

3.1 Inner Detector

The Inner Detector is the sub-detector that is the closest to the interaction point, and given its proximity, it must be the densest of the detectors in order to be able to distinguish all the different particles that result from the collision. It detects the traces left by charged particles when they cross it, which curve due to the generated magnetic field. The direction of the measured curved trajectory reveals a particle's charge sign, while the degree of curvature reveals its momentum. The tracker can also reveal secondary vertices, which indicate that a particle produced in the interaction point decayed afterwards into even more particles. The Inner Detector is further subdivided into the Pixel Detector, the Semiconductor Tracker (SCT), and the Transition Radiation Tracker (TRT), which can be seen in figure 3.2.

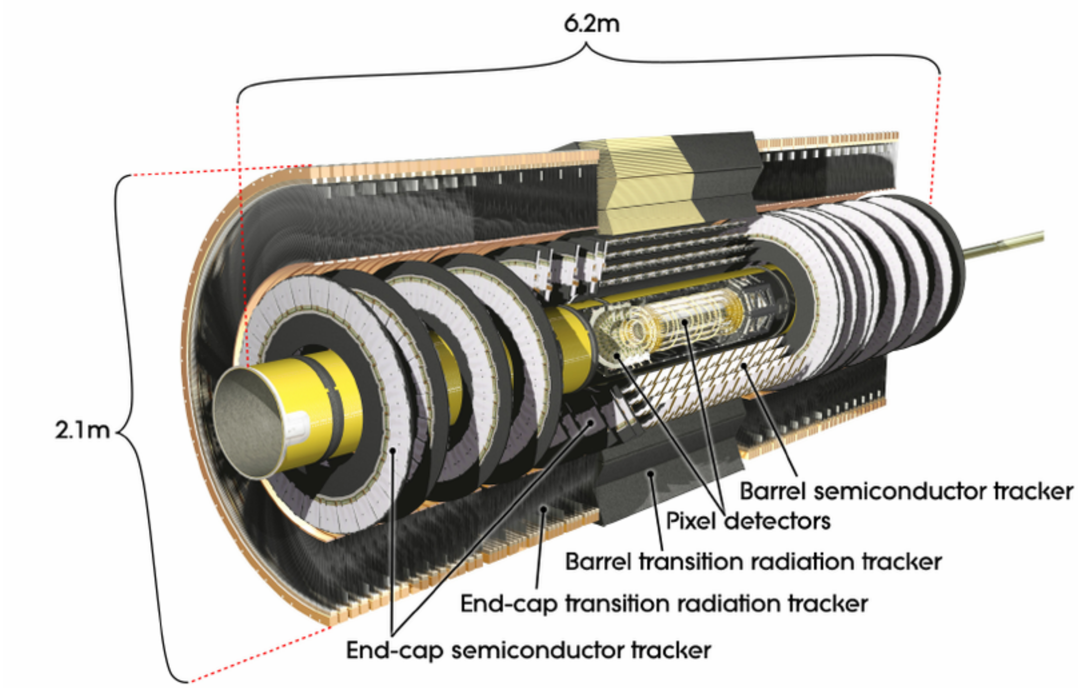

Figure 3.2: ATLAS Inner Detector. [3]

3.1.1 Pixel Detector

The Pixel Detector is the closest one to the interaction point. It consists of three concentric barrels surrounding the beam pipe, and three disks at the barrel caps, covering the whole angular spectrum. Together, they have a total of 1,744 modules, each containing approximately 46.000 pixels, giving a total of over 80 million channels. A single pixel is 50 by 400 μm in area, ensuring the resolution is enough to identify single tracks. Given the large amounts of radiation that the Pixel Detector is under, it has to be radiation hardened to be able to continue operating for the whole experiment duration.

3.1.2 Semiconductor Tracker

The SCT has a similar concept as the Pixel Detector, but instead of pixels, it is made of long, narrow strips. Each strip is 80 μm by 12 cm in area, and each module has 768 strips, covering an area of 6.36×6.40 cm^2. There are 4,088 two-sided modules, covering a total area of 60 m^2 over 4 cylindrical barrel layers and 18 planar endcap disks. With 6.3 million channels, it has the most critical tracking capabilities in the plane perpendicular to the beam axis, thanks to the strip's dimensions, as well as its larger area.

3.1.3 Transition Radiation Tracker

The TRT is the outermost component of the Inner Detector, and instead of using silicon, it uses drift tubes. These tubes are 4 mm in diameter and up to 144 cm long (hence the secondary name "straws"). Each straw is filled with a non-flammable gas mixture of 70% Xe, 20% CO_2 and 10% CF_4, and in its center, has a 0.03 mm diameter gold-plated tungsten wire. When a charged particle crosses the gas it ionizes it, and the electrons drift to the wire (which is held at about 1500 V), producing the signals. The wires with signals create the track of straws that were hit, which allows the path of the particle to be determined afterwards. There are 50,000 straws in the barrel, each 144 cm long, and 250,000 straws in both endcaps, each 39 cm long. This detector allows to tell apart charged pions from electrons, by looking at their transition radiation. Lighter particles (electrons and positrons) produce much greater transition radiation, and this will appear as larger and stronger signals.

3.2 Calorimeters

Going outwards radially after the Inner Detector come the calorimeters, which instead of tracking the particles, are designed to absorb them completely. The energy of the particle is deposited on the calorimeters, which sample the particle shower created during the absorption, and give a measurement of the energy. Each type of particle will have a different energy signature, and together with the information that the Inner Detector provides, results in most particles being identified and their properties measured. The calorimeters can be divided into two types, each focused on the measurements on a specific family of particles: the electromagnetic (EM) calorimeter, and the hadronic calorimeter. However, it's easier to describe the calorimeters based on their technology: the tile calorimeter and the liquid argon calorimeter. The different calorimeter types can be seen in figure 3.3. There are however, two known particles that are not contained by the calorimeters: the neutrinos and the muons (the way they are measured is explained in further sections).

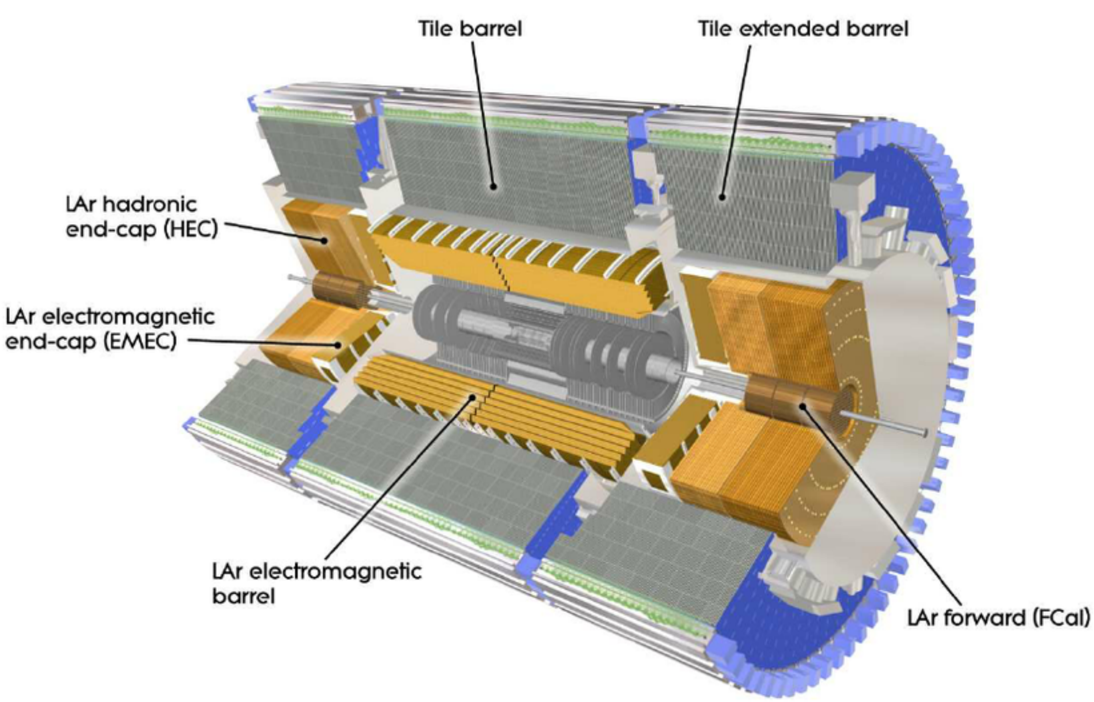

Figure 3.3: ATLAS calorimeters. The various sections are indicated, and the Inner Detector is visible inside. [3]

3.2.1 Tile Calorimeter

The Tile Calorimeter (TC) is part of the hadronic calorimeter, and covers the barrel region of ATLAS ($|\eta| < 1.7$).

The TC has a fixed central barrel, and two movable extended barrels. It is made of alternating steel and scintillating tiles, where the steel acts as the absorbing material, while the scintillating tiles are the sampling material. The tiles are readout by fibers that deliver the light to photo-multiplier tubes, which can detect small amounts of light and convert it into an electrical pulse.

3.2.2 Liquid Argon Calorimeter

Given the higher amounts of energy that are radiated towards the endcaps of ATLAS, the hadronic calorimeter there needs another type of technology to be able to measure the energies effectively, and thus Liquid Argon is used. Similarly, for the entirety of the EM calorimeter liquid argon is used as well.

The hadronic Liquid Argon (LAr) calorimeter is comprised of two parallel-plate copper/LAr endcap calorimeters that cover the region $1.5 < |\eta| < 3.2$. The EM LAr calorimeter has a barrel calorimeter consisting of two half-barrels, while the endcap EM calorimeter comprises two wheels, one on each side of the barrel.

The LAr calorimeter is made of accordion-shaped lead absorbers, with liquid argon gaps between them. Inside the gaps are copper-kapton electrodes. As the particles from the showers cross the gaps, they ionize the LAr and the electrons and ions drift to the grounded lead absorbers or the powered electrode, producing the electric signals that the readout electronics collect. In order for the argon to stay in liquid form, the calorimeter has to be cooled down to -183° C.

There is a final LAr calorimeter, called the Forward Calorimeter (FCal), which focuses on measuring particles in the forward region. The configuration is different from the one previously described, but the principle is the same. The FCal is made of three layers of absorbing materials (copper, tungsten and tungsten again), each with long narrow cathode rods. The rods are inserted into tubes, and have fibers that run along them in spiral, keeping a very thin gap for the LAr. The cathode and the tubes are held at a high voltage difference, so that when a particle crosses the gap, the LAr ionizes just like previously described. The tubes are positioned parallel to the proton beam and are embedded in a matrix, and the rods, tubes, and matrix are all made of the same absorbing material.

3.3 Magnet System

The Magnet System creates a very strong magnetic field inside the detector, so that the paths that charged particles follow are bent due to the Lorentz Force. This allows the other detectors to measure the curvature of their traces and with that their momenta, as described earlier. The Magnet System has three different sections, as can be seen in figure 3.4, and each one is designed so serve a specific purpose.

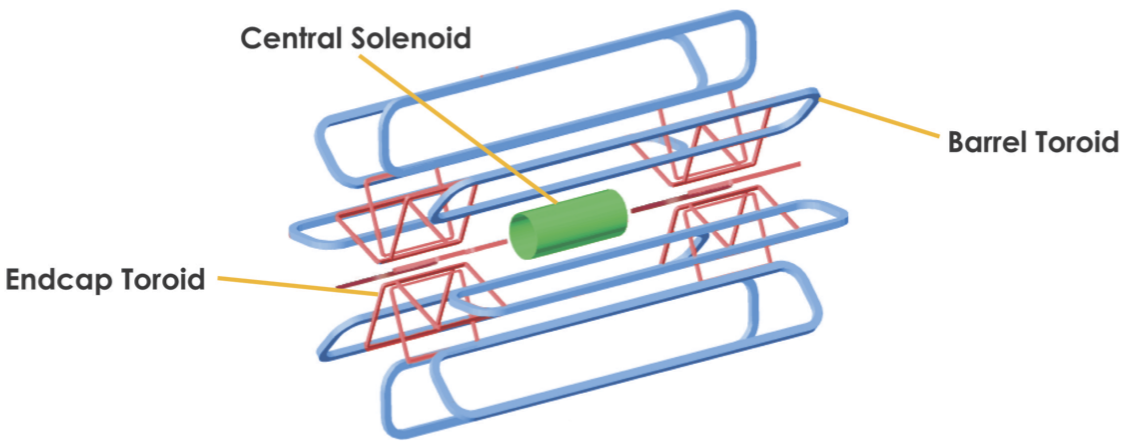

Figure 3.4: ATLAS Magnet System. The positions of the corresponding parts are indicated in their corresponding sections. [4]

3.3.1 Inner Solenoid

The Inner Solenoid surrounds the Inner Detector, and creates a nearly uniform 2 Tesla field inside, to ensure precise track measurements in the most sensitive part of the experiment. It is a 5.3 m long cylinder, with a diameter of 2.4 m, and walls only 4.5 cm thick. It has 9 km of superconducting cable, that makes a single coil with 1173 turns.

3.3.2 Barrel Toroid

The Barrel Toroid consists of eight air-core superconducting coils assembled radially and symmetrically around the beam axis. The coils are of a flat racetrack type with two double-pancake windings, which are housed in an aluminum alloy casing, while the coils are housed in individual cryostats taking up the forces between them. Each coil is situated just outside the calorimeters, but within the muon chambers, surrounding the ATLAS barrel. The field they produce is not as uniform as the one in the Inner Solenoid, due to the cost it would have creating a solenoid that large. They provide 2-6 T in the $0.0 < |\eta| < 1.3$ range.

3.3.3 Endcap Toroids

Similar to the Barrel Toroids, the Endcap Toroids consist of eight superconducting coils, only these ones are shorter and housed within the same cryostat. Each Endcap Toroid plugs the Barrel Toroid, completing the barrel. This design allows access to the inner parts of ATLAS, which is necessary to perform detector upgrades, or to replace parts that may fail due to radiation damage. The Endcap Toroids provide 4-8 T in the $1.6 < |\eta| < 2.7$ range.

3.4 Muon Spectrometer

Finally, the Muon Spectrometer measures the tracks of muons, which can go through the calorimeters, thus leaving no measurement for their energy. Accordingly, most muon detectors are placed at the outermost layers. In ATLAS, the barrel region of the Muon Spectrometer consists of three cylindrical layers around the beam axis, with parts of it both between, and on the eight coils of the superconducting barrel toroid magnet. The endcap region consists of other three circular layers or wheels, this time placed vertically, perpendicular to the beam axis. The innermost wheel is called the Small Wheel, and is placed in front of the end-cap toroid magnet. The middle wheel is called the Big Wheel, and is placed directly behind the end-cap toroid magnet. Finally, the outermost wheel is called the Outer Wheel, and is placed about 7.5 m further from the Big Wheel away from the interaction point. The various sections can be seen in figure 3.5.

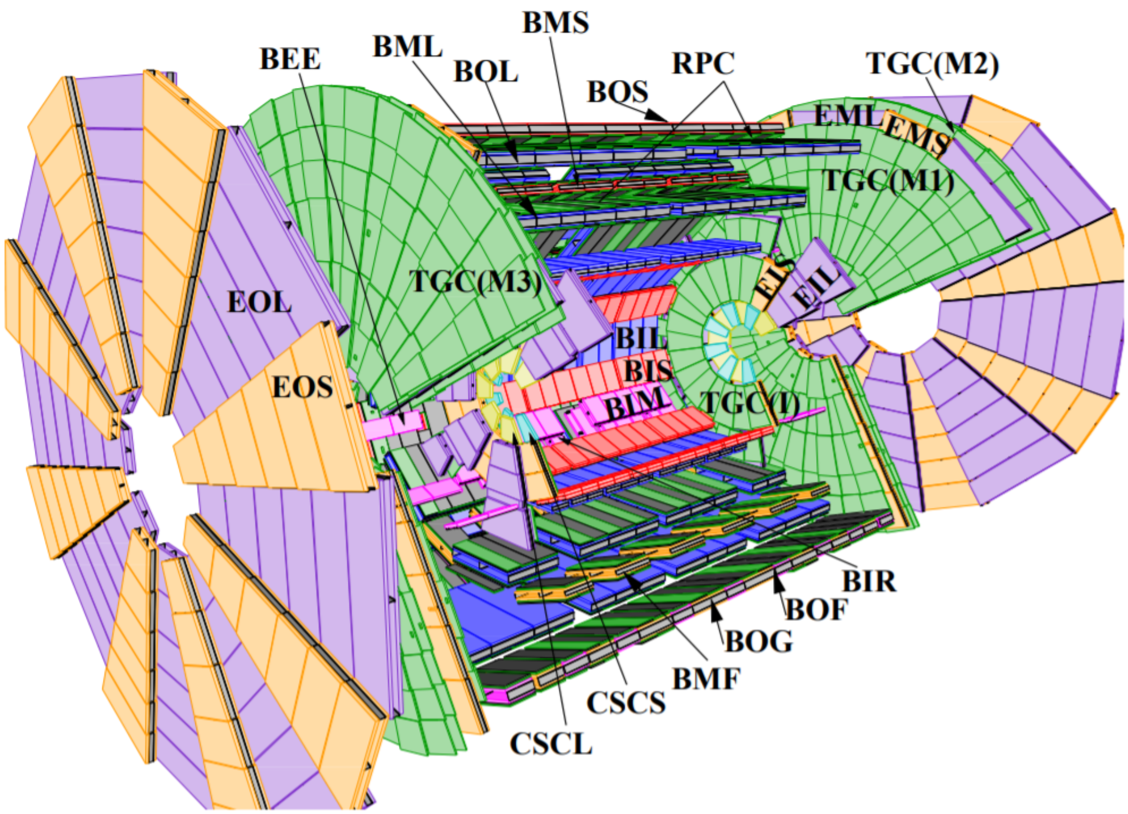

Figure 3.5: Muon Spectrometer. For MDTs, the naming convention for the first letter denotes region: barrel (B) or endcap (E). The second letter indicates the layer, inner (I), middle (M) or outer (O). The third letter indicates the sector type: small (S) or large (L). [3]

3.4.1 Monitored Drift Tubes

The MDTs make precision measurements of muon tracks along the barrel region, as well as in most of the endcap region. Their basic detection element are aluminum tubes, 30 mm diameter and with a 400 μm wall thickness, housing 50 μm diameter wires inside. They function similarly to the TRTs, having a 93% Argon and 7% CO_2 gas mixture inside, which ionize when a charged particle crosses them. In the innermost layer of the endcap region, the MDTs along the CSC (explained in the next subsection) form what are called the Small Wheels.

3.4.2 Cathode Strip Chambers

The CSCs make precision measurements of muon tracks on the part of the endcaps that the MDTs don't cover, which is the most forward region of the Small Wheel. This is due to their higher rate capability and time resolution. Instead of tubes, they have multiwire proportional chambers, with strip readout. The wires they use are aligned radially with the beam, while the strip cathodes are perpendicular to the wires, with the anode-cathode spacing equal to the anode wire pitch. This allows both coordinates to be measured from the induced-charge distribution.

3.4.3 Resistive Plate Chambers

The RPCs are responsible for the trigger on the barrel region. They are gaseous parallel electrode-plate detectors, without wires. They have two resistive plates which are kept parallel to each other at a distance of 2 mm by insulating spacers, forming a gas gap, which is filled with a mixture of $C_2H_2F_4$/Iso-C_4H_{10}/SF_6. When functioning, the electric field between the plates is about 4.9 kV/mm. The RPCs have both η and ϕ strips, with pitches of 23 and 35 mm respectively. Thus, the ionizing tracks produce pulses in both coordinates, allowing redundancy in the track measurement thanks to the three layers.

3.4.4 Thin Gap Chambers

Finally, the TGCs are responsible for the trigger on the endcap region, as well as the determination of the second, azimuthal coordinate to complement the measurement of the MDT's in the bending (radial) direction. The TGCs are multiwire proportional chambers that use a highly quenching gas mixture of CO_2 and n-C_5H_{12} (n-pentane) and in them, the ionizing tracks produce signals in both the wires and strips. The next section will cover the sTGCs of the New Small Wheel, which are the next generation of this same technology.

Part II

Cosmic Ray tests for the QS1 module of the ATLAS NSW

The ATLAS detector, located in the main ring of the LHC, is planned to receive an upgrade during the Long Shutdown 2 (LS2), which will elapse from 2019 to 2020. The current Small Wheels, which are the inner muon detectors inside the end-cap region, will be replaced with the New Small Wheels (NSW). The NSWs will address some of the issues that the Small Wheel is currently facing and which will worsen when the luminosity and energy of the LHC are ramped up to their design values. The NSW will have such a cost and complexity, that it is too much for only one institution to manage and construct, so the tasks were divided among various member countries. In Chile specifically, two institutions are working in a joint collaboration to build and test part of the NSW. The Technical University Federico Santa María (UTFSM) is in charge of the main construction, and the Pontifical Catholic University of Chile (PUC) is in charge of the final construction details and the subsequent testing. The following chapters explain more details about the New Small Wheel, its construction and testing work done to them.

Chapter 1

The New Small Wheel

Right now, the current Muon Tracking System along the endcap regions of ATLAS makes use of three structures: the Outer Wheel, located in the outermost layer of the detector, the Big Wheel, located right outside the Endcap Toroids, and the Small Wheel (SW), which is located in between the Endcap Toroids and the inner part of the detector (see figure 1.1).

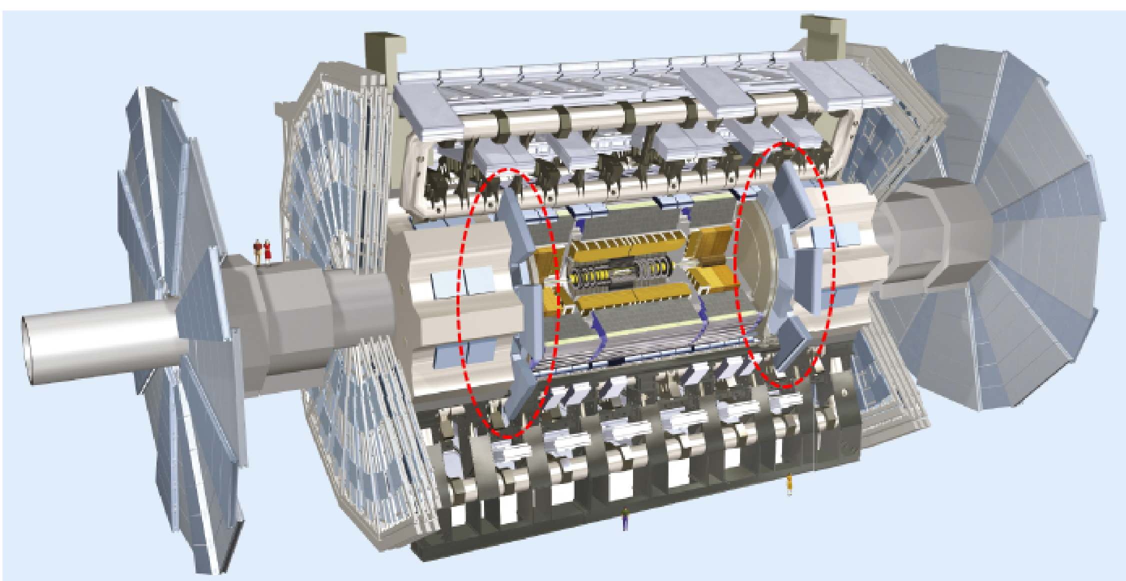

Figure 1.1: Location of the Small Wheels in the ATLAS experiment. Alongside the Big and Outer Wheels, these detectors measure the momenta of the muons along the endcap region.

The Small Wheels are planned to be replaced by the NSWs by the end of LS2, due to 3 main reasons. First, the current SW trigger has no tracking capabilities, which means that often fakes are measured(see figure 1.2). The NSW trigger will be based track segments, which will allow a better efficiency in identifying fakes. The second reason is that it will also improve the momentum resolution due to the better track information of the muons. Lastly, the upcoming High Luminosity upgrade that will be done on the LHC will mean that the current trigger capabilities of the SW will be insufficient to be able to cope with the extremely large rate of events, the NSW will have a much faster trigger rate, which will allow the muon detection system to work even under the High Luminosity regime.

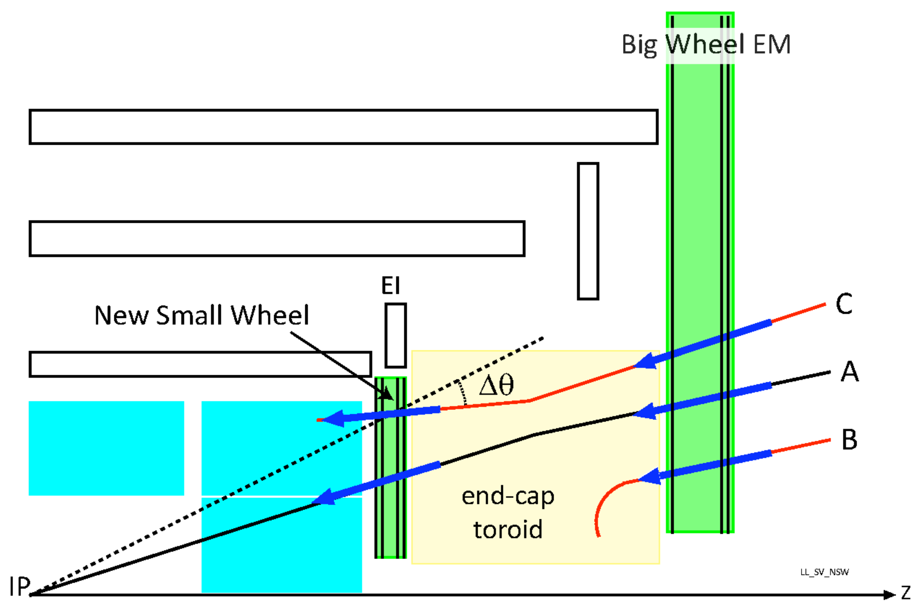

Figure 1.2: Schematic drawing of a quarter of the ATLAS detector with possible trigger tracks in the endcap region. Particle A leaves a track in all detector regions and points towards the interaction point. Particle B gives only a signal in the Big Wheel and Particle C does not point towards the interaction point. Only Particle A corresponds to an acceptable muon. [5]

The NSW is subdivided into sectors, similar to how one would divide a pizza. There are two sector sizes: large, and small. Each sector will have two chamber technologies, one primarily devoted to the Level-1 trigger function (small-strip Thin Gap Chambers, sTGC) and one dedicated to precision tracking (Micromegas detectors, MM). Such a precision is crucial to maintain the current ATLAS muon momentum resolution in the high background environment of the upgraded LHC. The MM chambers can, at the same time, confirm the existence of track segments found by the muon end-cap middle station (Big Wheels) online. The sTGC also has the ability to measure offline muon tracks with good precision, so the sTGC-MM chamber technology combination forms a fully redundant detector system for triggering and tracking both for online and offline functions. This detector combination has been designed to be able to also provide excellent performance for the eventual High Luminosity LHC upgrade.

1.1 Small-strip Thin Gap Chambers

Each sector has two wedges of each chamber technology. There are two MM wedges in the middle, sandwiched between two sTGC wedges. A wedge is the assembly of smaller detectors, the sTGC wedges in particular are each subdivided into 3 modules. The large wedge is made of the QL1, QL2 and QL3 modules, while the small wedge is made of the QS1, QS2, and QS3 modules. The number increases as one gets further from the center. Finally, each module is a stack of four sTGCs. A single gas gap is called a singlet, and the 4-stack is called a quadruplet, hence the "Q" on the module names (see figure 1.3).

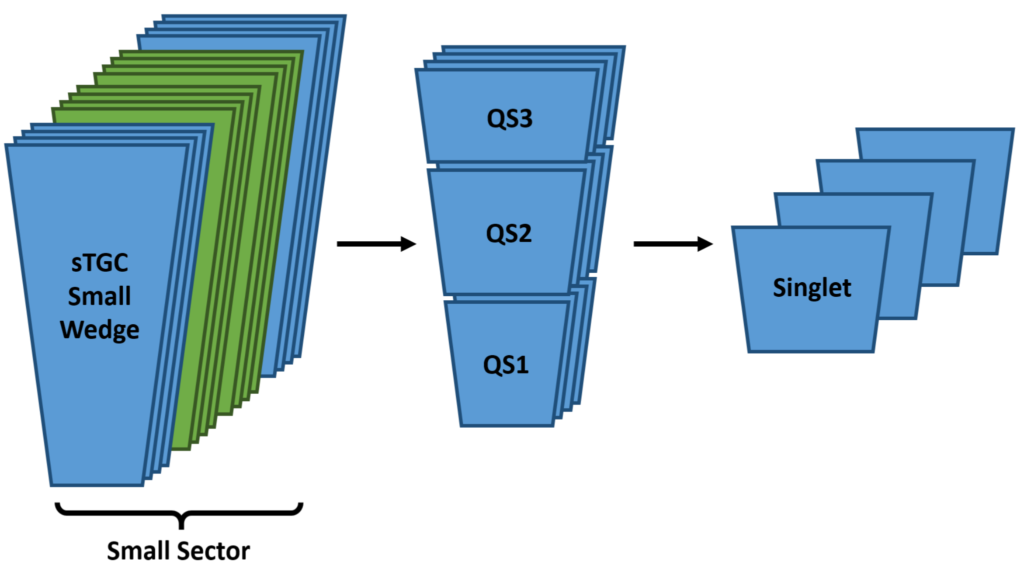

Figure 1.3: Diagram of the Small Sector structure. The Large Sector has is similar, only that the wedges are wider. The sTGC wedges are in blue, while the MM wedges are in green.

The TGC system, used in the present ATLAS muon endcap trigger system, has gone through a long phase of R&D and testing. The basic detector design for the NSW has two quadruplets 35 cm apart in z. Each quadruplet contains four TGC's, each with pad, wire and strip readout. The pads are used to produce a 3-out-of-4 coincidence to identify muon tracks roughly pointing to the interaction point. They are also used to define which strips are to be readout to obtain a precise measurement in the bending coordinate, for the online muon candidate selection. The azimuthal coordinate, where only about 10mm precision is needed, is obtained from grouping wires together. The charge of all strips, pads and wires are readout for offline track reconstruction.

The basic Small strip Thin Gap Chamber (sTGC) structure is shown in figure 1.4. It consists of a grid of 50 μm gold-plated tungsten wires with a 1.8mm pitch, sandwiched between two cathode planes at a distance of 1.4mm from the wire plane. The cathode planes are made of a graphite-epoxy mixture with a typical surface resistivity of 100 k$\Omega/\square$ sprayed on a 100 μm thick G-10 plane, behind which there are on one side strips (that run perpendicular to the wires) and on the other pads (covering large rectangular surfaces), on a 1.6mm thick PCB with the shielding ground on the opposite side. The strips have a 3.2mm pitch, much smaller than the strip pitch of the ATLAS TGC, hence the name 'small-strip TGC' for this technology.

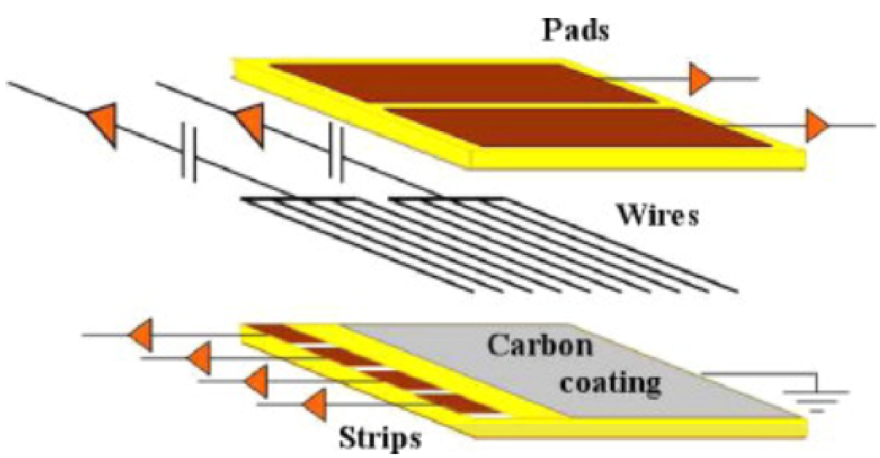

Figure 1.4: Basic sTGC structure. The pads, wires and strips form a singlet. Four alternating singlets form the complete quadruplet. [5]

When a charged particle crosses the sTGC, the n-Pentane/CO_2 mixture in the chamber is ionized. The electrons are drawn to the HV wires and produce a signal. Meanwhile, the Ions drift to the conducting walls (pads and strips) and capture electrons from them causing another pulse with different polarity. In that way, there are 3 types of signals: wires, strips, and pads. The pads, with their large rectangular shapes, give the general location of the hit, which reduces the number of strip data that is read out. This allows for much more efficient trigger system, one of the main purposes of the sTGCs. The strips charge clusters are used to calculate a centroid, and the two centroids (one from the pivot quadruplet, and one from the confirmation quadruplet), are used to create a track segment. This can later be used to crosscheck with the tracking capabilities of the Big Wheel to determine which tracks come from the interaction point, and which ones might be fake (see figure 1.2).

1.1.1 Construction

Even though the construction is done in Valparaíso, the process is shortly outlined in this section. Each layer of an sTGC is built separately. First, the boards are cleaned and prepared to be worked on after their transport. The pad and the strip cathodes are sprayed with graphite. Once the graphite has set, spacers are placed to form the gas gap, and the wires are winded on one of the cathodes. Then, using a vacuum table, the cathode with the wires is laid flat, and the other cathode is glued on top. After a singlet is completed, it goes though a series of tests, and if everything is as expected, it can be glued to another singlet to make a doublet. The doublet must go through tests again, and if those tests are successful, it can be glued to another doublet to finally create a full quadruplet. After the quadruplet is tested for a final time, it can move to the next phase of its construction: the soldering of the adapter boards.

1.1.2 Electronics

The pulses produced in the pads and strips travel through copper lanes to small cathode terminations on the sides of the module. In order to readout, process and digitize the signals, various electronics are added to the modules. This is one of the main tasks that PUC has to perform in the construction of the QS1 modules.

Adapter Boards

Having the signals on the full length of the module isn't practical, so adapter boards are soldered to its sides to funnel the signals into smaller and more dense connectors. For a single layer, a strip Adapter Board (sAB) is soldered on one side, while a pad Adapter Board (pAB) is soldered on the opposite side. This includes over 450 terminations per layer, as well as copper tape connecting the grounds of the cathodes to the grounds of the adapter boards. In total, a full quadruplet will have 8 ABs, 4 on each side. The soldering is tested by doing pulser tests, which consist of sending a pulse through the wires, and then checking the connectors on the ABs to test that the pulses are seen on all the channels that are soldered.

Figure 1.5: Curing of the epoxy glue on the wires 0 Adapter Boards.

On the other hand, the wires also carry signals to the bases of the trapezoid. These signals must also be funneled into smaller connectors, which then connect to further electronics. For that, wires Adapter Boards (wAB) are used. The number and the characteristics of these wAB depend on the module type. For the QS1 specifically, the smaller base has the wires 0 Adapter Boards (w0AB), which only deliver High Voltage to the wires, and do not actually readout signals. These w0ABs are first soldered to the actual wire terminations coming out of the module, and after that, the boards are permanently attached to the module using epoxy (see figure 1.5), which prevents sparks due to the high voltage (HV). Before proceeding, HV is applied to the wires to test the epoxy, which should have no sparks. Now, on the larger base, first come the wires 1 Adapter Boards (w1AB), which are soldered and glued with epoxy similarly to the w0ABs (the HV test is repeated on this side as well), and on top of them, a single wires 2 Adapter Board (w2AB) is attached with screws, meaning that this board could be removed if needed. Together, the w1ABs and the w2AB deliver High Voltage to the wires, and also funnel the signals from the wires to connectors on both ends of the w2AB. From the w2AB, a Flexible Flat Cable is used to connect to the pAB, which means that the connector on that board, actually contains both pad and wires signals.

After this, the construction is considered to be finished. However, before shipping to CERN, the module has to be tested. For that, even more electronics are attached to the module.

Front End Boards

With all the ABs installed on the module, one has the signals condensed in small connectors on the ABs. In order to readout data, various Front End Boards (FEBs) are connected to the ABs (figure 1.6). There are two types of FEBs used. The ones that connect to the pAB are called pad Front End Board (pFEB), and have only one connector. Even though they are called "pad" Front End Boards, they also process the wires signals, since they are taken from the wires, through the w1ABs and w2AB to the pAB. The FEBs that connect to the sAB are called strip Front End Board (sFEB). They have two connectors, given the higher amount of strip channels the module has.

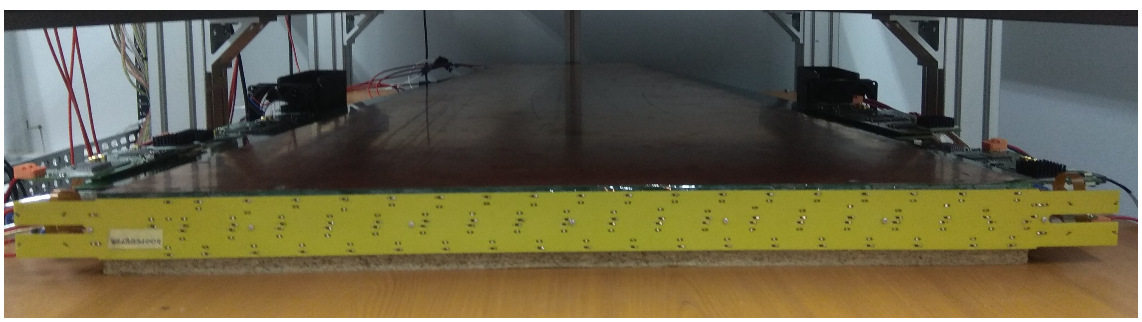

Figure 1.6: Full QS1 module, with ABs soldered and glued, as well as all FEBs attached. The module is on the hodoscope (explained below), ready to be tested.

In summary, in order to be able to readout data from all pads, strips and wires, a full quadruplet needs:

- 4 pad Adapter Boards and 4 strip Adapter Boards soldered to the module,
- 4 wires 0 Adapter Boards attached on the small base,
- 4 wires 1 Adapter Boards attached to the large base, and 1 wires 2 Adapter Board attached to the wires 1 Adapter Boards,
- 2 flat cables connecting the wires 2 Adapter Boards to the pad Adapter Boards,
- 4 pad Front End Boards attached to the pad Adapter Boards, and the 4 strip Front End Boards attached to the strip Adapter Boards.

This is still not considering the DAQ system, which will be explained in the next chapter.

Chapter 2

Cosmic Ray tests

Production of the sTGCs is divided between 5 countries: Canada, Israel, China, Russia and Chile. Part of the construction process is the efficiency mapping of the quadruplets. For this, all quadruplets are tested using cosmic rays at the mentioned production sites before shipping them to CERN. The cosmic ray scan provides in first place a very basic functionality test by reading the hits on strips, pads and wires. It also provides a full map of their efficiency, and a rough measurement of the position resolution ($\sim$400 μm). The cosmic-ray set-up includes two Plastic scintillator arrays above and below the test volume. They track the cosmics through the quadruplets under test and provide the trigger signal needed for the data acquisition system. The pads of every detector plane are readout and if a hit is observed in the expected incident point, this is used for the calculation of the local efficiency. A mapping of the detector efficiency for every point is produced. Furthermore, the charge in the strips of every plane is also readout and their centroids are calculated. Comparison of the position in two adjacent planes gives the average resolution (within a given pad) to better than 400 μm. The efficiency maps and the average resolution for every pad on a given plane are recorded in a centralized database system. A quadruplet is considered acceptable if each of its planes has an efficiency exceeding 95% on 95% of its sensitive area.

2.1 Trigger System

2.1.1 Scintillator Array

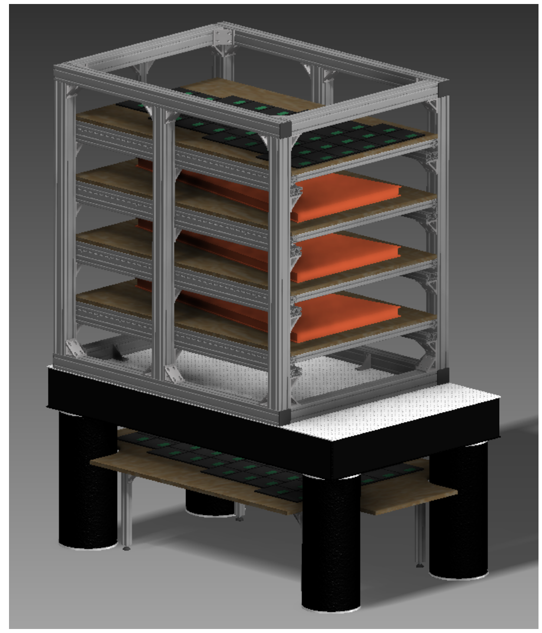

Figure 2.1: Diagram showing the scintillator array placement, and three modules that can be tested or stored in the hodoscope.

In order to provide the data acquisition system with precise trigger signals, the muons must be measured with another detector first. By placing one of those detectors on top of the module and another one below it, a confirmation system is created: when a muon passes through both of them, there is a coincidence in the signals of the confirmation detectors, and with that information the module can be triggered to make a measurement as well.

For this purpose, two arrays of plastic scintillators are placed above and below the module to be tested (see figure 2.1). Just like the module, plastic scintillators can also measure charged particles, although the way they function is different, and is explained in more detail in the next section. For the setup a hodoscope is used, in order to have an easy way to place the sTGCs and the scintillators in the cosmic ray testing system. The scintillator arrays have a shape that is as close as possible to the module. This is done to cover the area of the module completely, as well as to avoid fake triggers from particles that may cross outside the module but still hit two scintillators.

2.1.2 Plastic scintillator

A scintillator is —as its name suggests— a material that "scintillates" (i.e. emits light) when it is excited by ionizing radiation. There are many types of scintillators, but here the focus is on plastic scintillators, since that is what is used in the setup previously described. A plastic scintillator consists of a primary fluorescent emmiter, called the "fluor", suspended in a polymer, called the "base". Optical fiber is placed inside the polymer

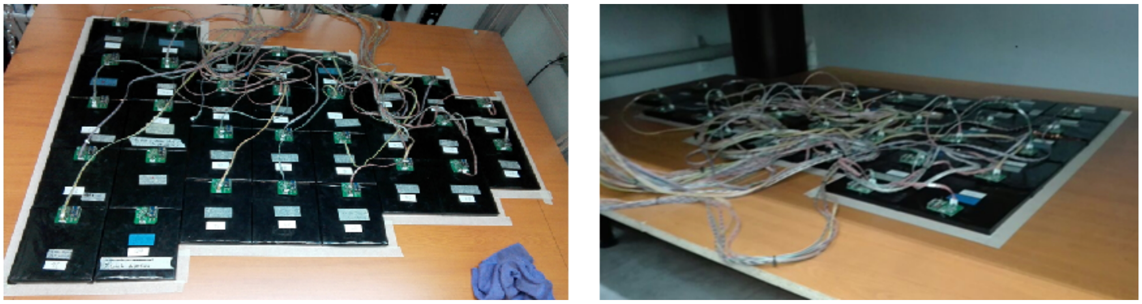

Figure 2.2: Plastic scintillator arrays. On the left is the top array, and of the right the bottom one. The distribution of the scintillators approximates the trapezoidal shape of the module.

during the construction, along with a multi-pixel photon counter (MPPC) on one of its ends. That way, when ionizing radiation excites the plastic, the light pulse is collected by the fiber and directed to the MPPC, which converts it into an electrical signal. Depending on the material, the MPPC might need to have a voltage applied in order to observe a signal, since the photons absorbed from the scintillation might not be enough.

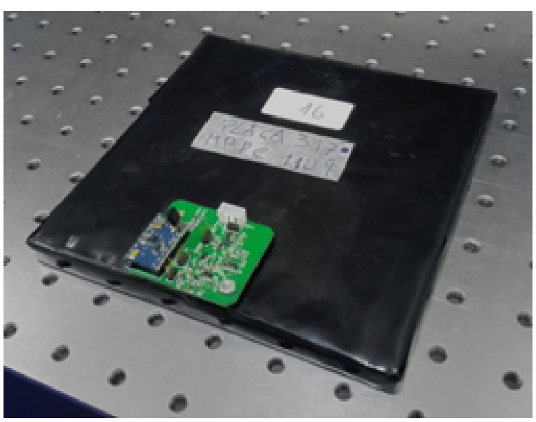

Figure 2.3: Single plastic scintillator. The circuit board connects to two pins on the scintillator, and a black protection is used to cover the plastic from light, so that only particles may produce a scintillation.

In this setup, plastic scintillators with a square shape are used, which are 15 cm long on their sides, and 2 cm high (figure 2.3). Each scintillator also has a tiny circuit board that digitalizes the analog pulse created by the MPPC. In order to function properly, the boards have to be powered with 5 Volts. Once powered, a potentiometer controls the voltage inside the plastic scintillator, between 60 and 70 Volts. If this voltage is too high, the MPPC will be triggered with ambient radiation or even thermal noise, resulting in high noise rate. If it is too low, it will only trigger with very energetic particles, or simply not at all. The voltage value for which the efficiency is maximum, while having the lowest rate (lowest noise) is what is called the “optimal point”. The optimal point has to be found beforehand, in order to leave each scintillator in its ideal working voltage before being placed in the hodoscope. However, since each scintillator has minute differences in its production, circuit board, etc, the optimal point has to be determined on a case-by-case basis.

This was done using a scintillator "sandwich" (figure 2.4). Using the same principle that will be used to measure the efficiency of the sTGC, one scintillator is placed on top the scintillator which will have its efficiency measured, and another one is placed below. A smaller Field-Programmable Gate Array (FPGA, explained in the next section) was used to process the data, and to build an Efficiency vs Voltage curve for each scintillator.

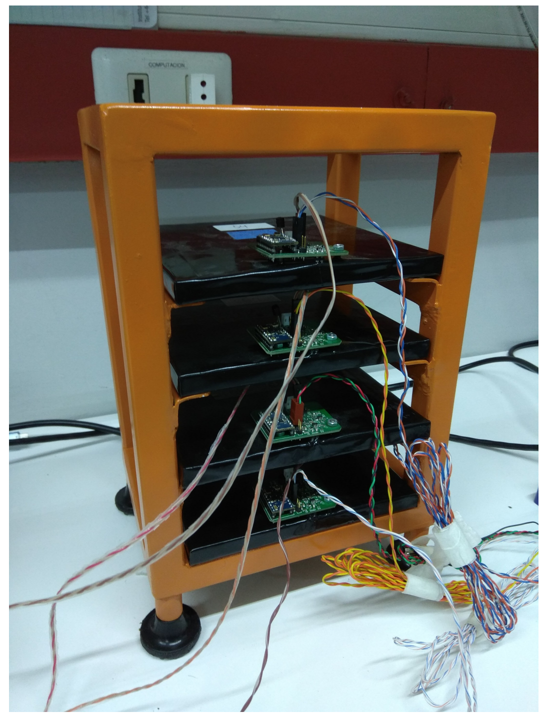

Figure 2.4: Scintillator "Sandwich". The scintillators on the top and the bottom are used as confirmation, while the middle ones are having their efficiency measured.

The results showed that there were scintillators that reached the optimal point before others even started measuring. By continuing to raise the voltage, the scintillators that weren't measuring would reach their respective optimal points, however the rate of the previous ones would've risen to values too high to still be considered at their optimal point. These results can be seen in figure 2.5.

While this method is very precise, it can't be done to a scintillator while it is in the cosmic ray stand. So, in order to avoid problems with calibration during the cosmic ray measurements, and having to check the individual optimal points of the scintillators constantly during their use, a simpler calibration method was considered necessary.

The second method was motivated by the idea that the optimal points of the scintillators might be correlated with the measuring rate they displayed. It was found that at around a 15 Hz rate, most scintillators reached their optimal point, as can be seen in figure 2.6. This was first observed in a group of scintillators, and then was tested on scintillators for which their efficiency curve had not measured yet. It was found that on the new scintillators, setting the rate immediately at around 15 Hz, would give very good efficiencies. This information is what was used to monitor and recalibrate the scintillators when they were already installed in the cosmic ray test system.

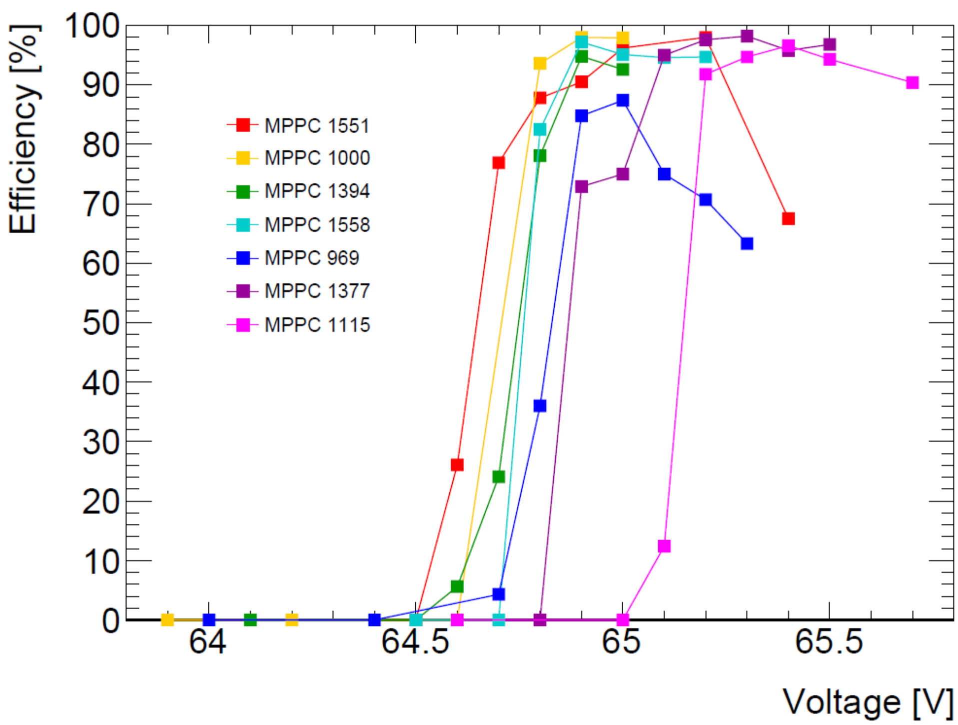

Figure 2.5: Efficiency vs voltage plot. It can be seen that different scintillators have different efficiencies at different voltages, making this a poor parameter to find the "optimal point".

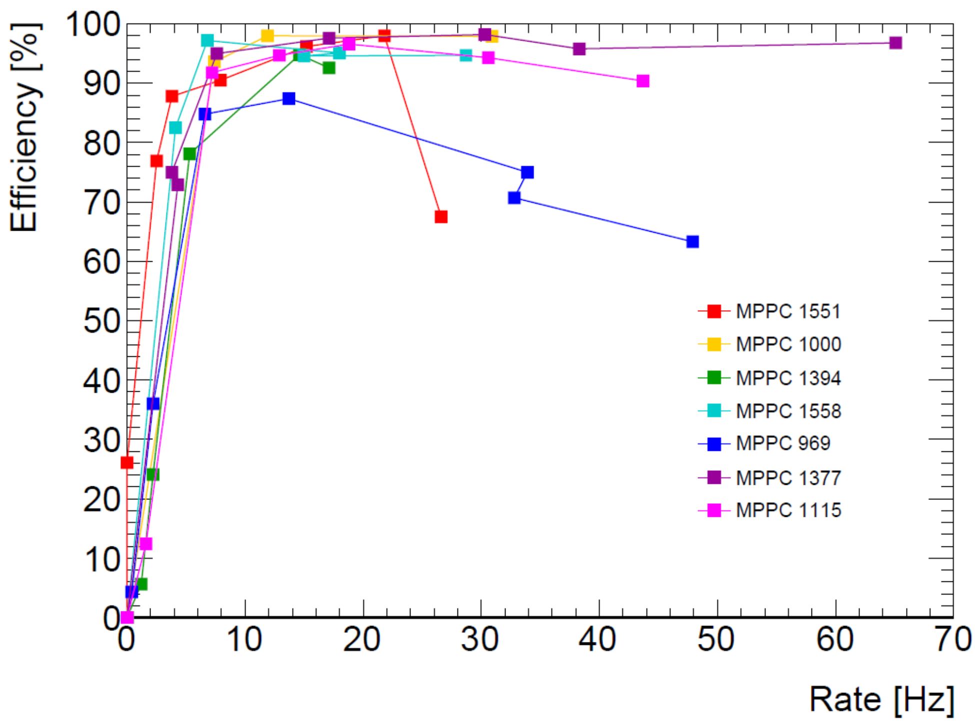

Figure 2.6: Efficiency vs rate plot. It can be seen that different scintillators have reach a high efficiency starting from 10 Hz. This makes rate the chosen parameter to find the "optimal point".

2.1.3 Field-Programmable Gate Array

With all the scintillators in place, the coincidences could be measured, in order to see if any muons crossed the two arrays. The signal pulses from the scintillators are sent to a Saturn Spartan 6 Field-Programmable Gate Array (FPGA, figure 2.7) which processes the signals and checks if there is a coincidence between any of the scintillators on the array on top, and the ones on the bottom. If there is one, that tells us that a particle must have crossed the module, so a trigger signal is sent to the DAQ.

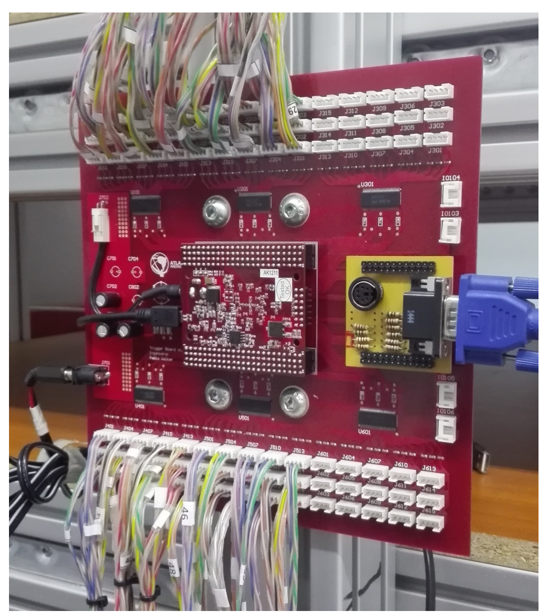

Figure 2.7: Field-Programmable Gate Array. Cables go to the top and the bottom scintillator arrays.

An FPGA is preferred in this case to a microprocessor, since it is capable of handling data in a parallel manner instead of serial, which allows for a much faster time between input and output signal. Apart from handling the coincidence check, the firmware in the FPGA was programmed to output to a VGA display, seen in figure 2.8. On the left side, it shows the instant frequencies of the scintillators (which includes muons as well as noise). This is used to do the monitoring and recalibration mentioned before. On the right side, the VGA display shows the instant muon rates on each scintillator (i.e. just muons, no noise). This is done by matching the coincidences to the signals that triggered that coincidence, and counting only those ones. The result is that it can be seen in real time if the scintillators are actually measuring muons, and if one of them shows no muons, it means that the total rate that is seen on the left side is pure noise and the scintillator has to be checked.

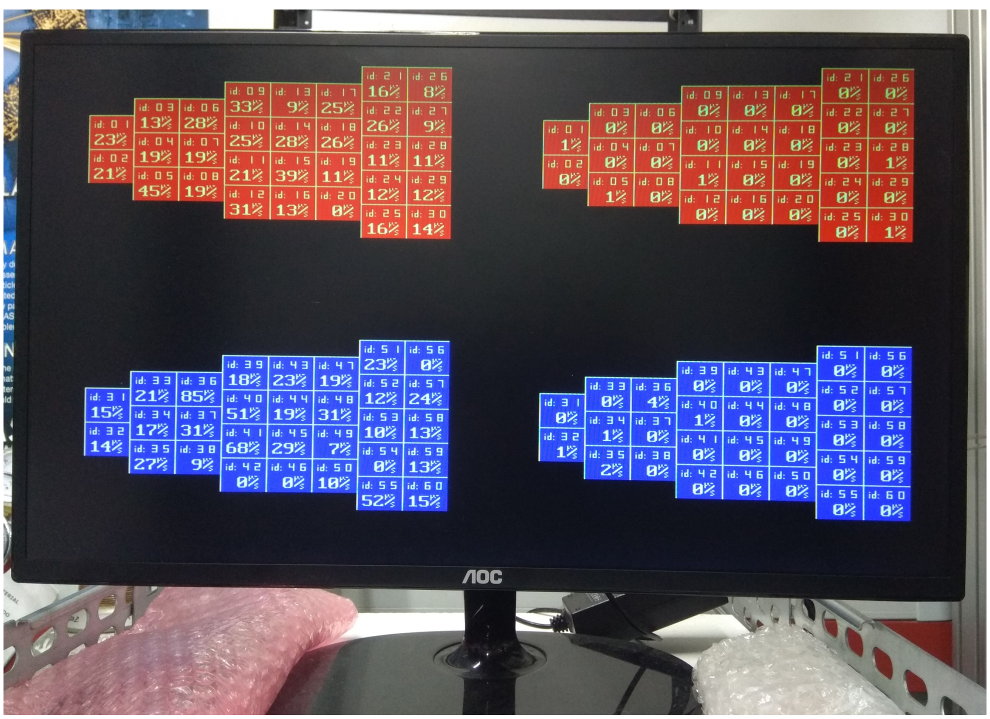

Figure 2.8: VGA display showing the instantaneous rate of each scintillator on the left, as well as the muon rate on each of them on the right. The red indicates the upper array, while the blue indicates the lower array.

2.2 Data Aquisition

2.2.1 Experimental Setup

As mentioned in section 3.1.2, in order to obtain the pulses produced by the sTGC module, Adapter Boards (ABs) are soldered to the cathode terminations on the sides of the detector. These ABs funnel all the signals into more condensed connectors, specifically one GFZ connector on a pad AB, and two on a strip AB. Then, Front End Boards (FEBs) are attached to these connectors (see figure 2.9), which process the signal, amplify them, digitize them, and then send the data to the main DAQ FPGA, a KC705.

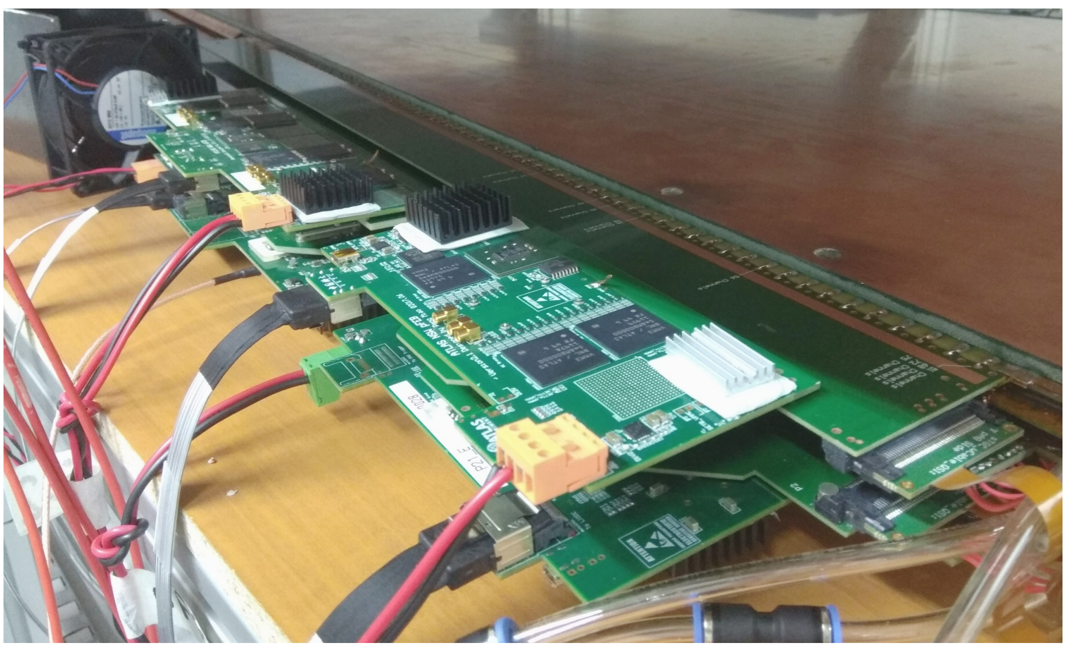

Figure 2.9: Front End Boards attached to the Adapter boards on one side of the module.

The DAQ system is comprised of an KC705 FPGA, which uses an FMC connector to connect to a so-called miniSAS-FMC board (figure 2.10). This miniSAS-FMC board is a custom made board which receives the connections from all the FEBs through silver twinax cables, and sends them to the FPGA through the FMC connector. The miniSAS board also recieves the trigger signal from the Saturn Spartan 6. This trigger input that the DAQ system recieves must be in a LVDS format, which is easily configurable in the Saturn Spartan 6 firmware.

In order to set the KC705 FPGA to readout data, it is necessary to connect it to a PC using a LAN cable. With the readout software (explained in the following subsection), one can send instructions to the FPGA so that it can establish communication with all 8 FEBs, making sure there is a proper synchronization, and also providing the FEBs with their respective configurations. This allows us to set specific configurations to each of the readout channels, such as the signal baseline, the threshold used to determine a hit, the gain used to amplify the signal, among others.

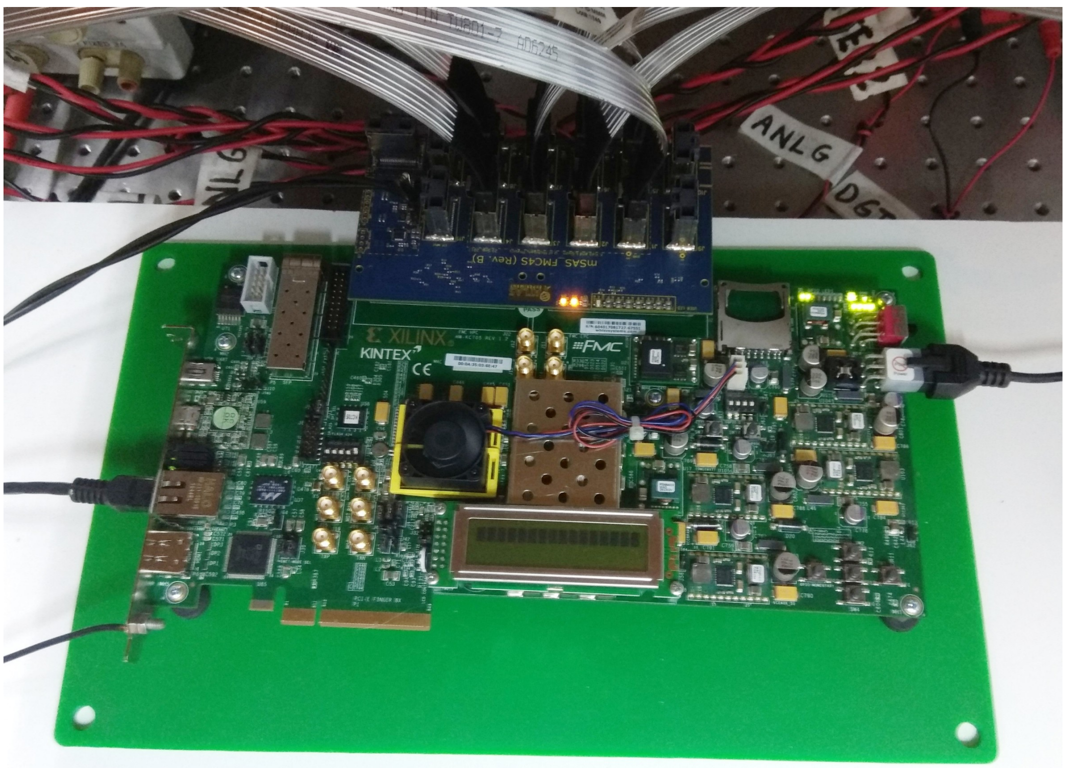

Figure 2.10: KC705 FPGA with the miniSAS-FMC board attached.

In summary, with the signals from the FEBs, the trigger from the Saturn Spartan 6 FPGA, and the connection to the PC, the KC705 FPGA is able to detect hits, build events, and send this information to the PC in order to be analyzed later.

For the construction process though, the FEBs are only temporarily installed on the ABs, and after the cosmic ray tests are perfomed, they are removed and the module is shipped only with the adapter boards attached. The same FEBs are later used for all the subsequent cosmic ray tests.

2.2.2 Readout Software

In order to be able to communicate with the FEBs, the PC must use a dedicated software (made by the University of Science and Technology of China team), which sends instructions to the FPGA, which in turn sends those instructions to the FEBs. In order for the system to work, the FEBs need to synchonize with the FPGA, the channel thresholds have to be callibrated, the gain must be set, among other things that are beyond the scope of this document (see figure 2.11).

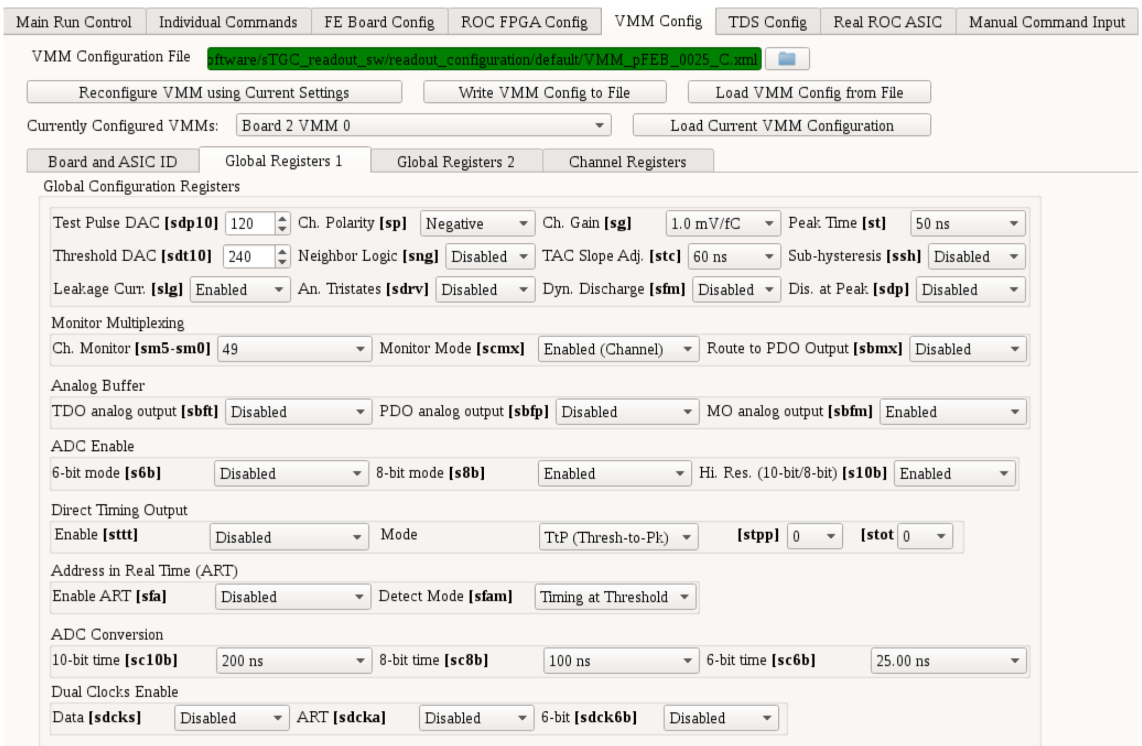

Figure 2.11: Readout Software. Various options can be seen, and each one of them can affect the measurement.

2.2.3 Monitoring Software

Another dedicated software, however this one is optional, and allows the user to monitor the data being saved in real time. Made by collaborators from the University of Michigan, this software allows to see hitmaps, PDOs, and other information beyond the scope of this work (see figure 2.12). It is used in conjunction with the readout software to run the cosmic ray tests.

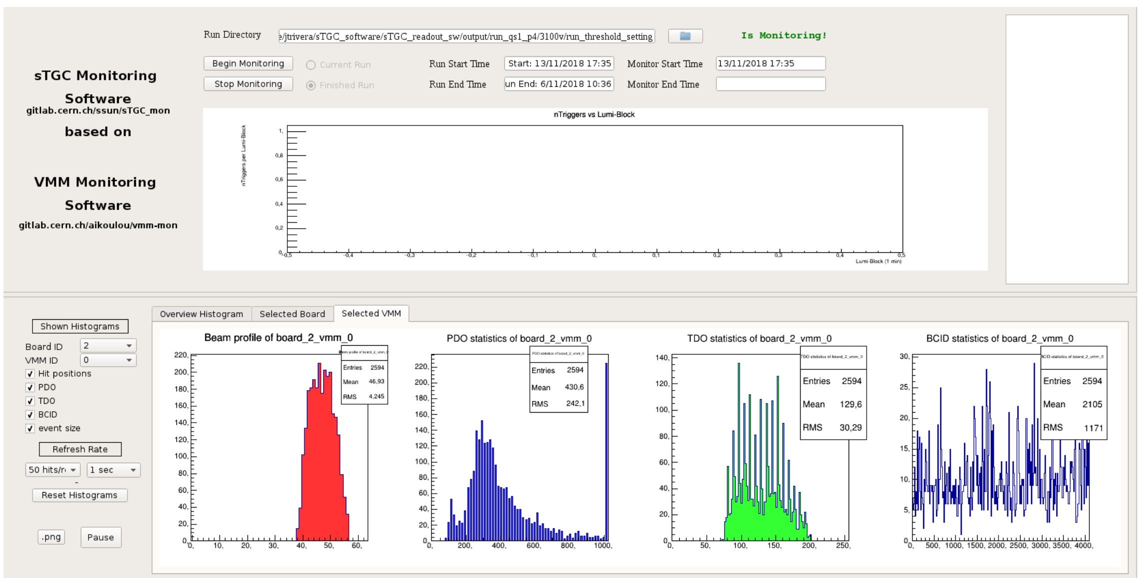

Figure 2.12: Monitoring Software. In this example, wires signals are being monitored, and the first plot on the left shows their hitmap.

Chapter 3

Results

3.1 Hit Maps

Using the data from the DAQ, the first information that can be extracted are the hitmaps of the strips, pads and wires of each layer. These hitmaps show the number of hits per channel during the duration of the measurment run, an example can be found in figure 3.1.

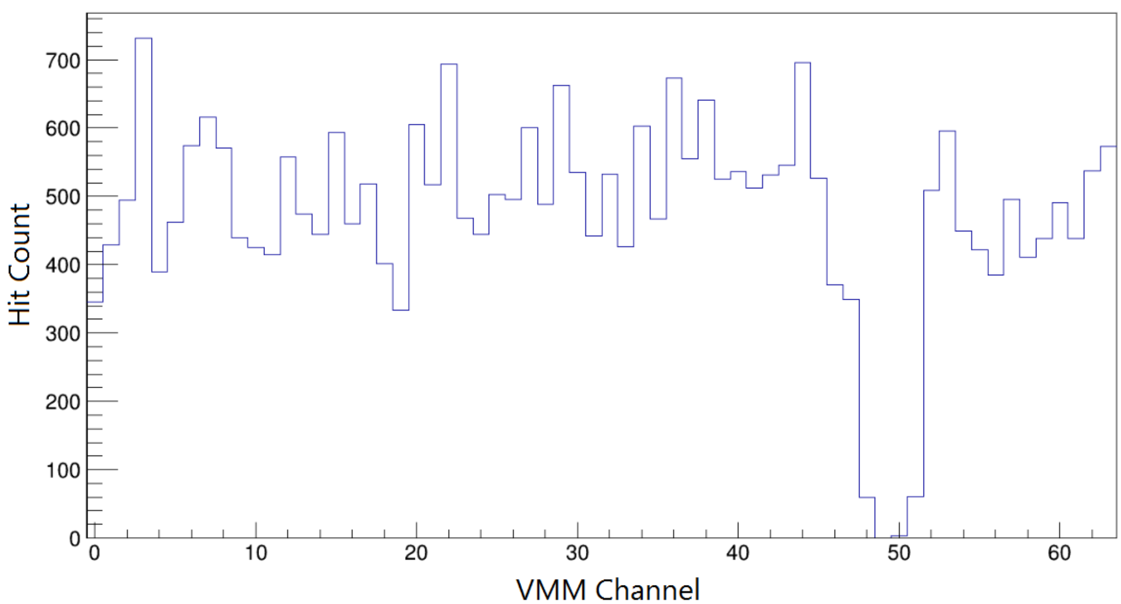

Figure 3.1: Hitmap of a single sFEB VMM. The dip on the left is due to a separator which keeps the cathodes apart, mantaining the shape of the gas gap. The decrease in efficiency there is expected.

The hitmaps allow an initial diagnosis of the module: one can see which channels might be dead, which ones are noisy, and even which channels might have a short-circuit between them.

3.2 Efficiency Measurements

With a more exhaustive analysis, efficiencies for pads and strips can be calculated. Knowing the pad and strip layout, the muon hits can be extrapolated or interpolated to all the cathodes they should have hit, and with that, the ratio of (particles that were detected/particles that *should* have been detected) can be obtained. For the first module sent to CERN, the average efficiency measurements per layer for the pads were:

Layer	Efficiency (%)
1	76.6
2	77.4
3	77.3
4	81.8

Table 3.1: Average efficiency per layer for the pads of the first module sent to CERN, with reference number QS1.P2.

With more experience, improvements were made to the measurements, specially in regards to the threshold setting, which has a large impact on the efficiency of the cathodes. This meant, that for the next module, the efficiencies measured improved:

Layer	Efficiency (%)
1	91.7
2	94.2
3	92.6
4	90.2

Table 3.2: Average efficiency per layer for the pads of the second module produced, with reference number QS1.P4.

The latest module is currently undergoing further tests, and will be shipped to CERN in the coming weeks.

Part III

Prospects on the search for heavy vector triplet bosons in the leptonic decay channels with the ATLAS Experiment at the HL-LHC

Given the current understanding of physics, it is known that the Standard Model is incomplete. It fails to explain many phenomena, such as the neutrino mass, gravity, dark matter, etc. However, given how well the data fits to the phenomena that it does explain, most new theories are extensions to the Standard Model, known as Beyond the Standard Model (BSM) theories, which just add to what the SM already has. Many of these extensions feature extra U(1) or SU(2) symmetries, which in turn, correspond to extra heavy vector bosons, similar to the Z and W bosons from the SM. These new bosons, often called Z' and W', would manifest as narrow resonances through their decays, with the leptonic channels being the easier ones to see . One of these models, the Sequential Standard Model (SSM), posits Z' and W' bosons with couplings to fermions which are identical to the SM counterparts. This model is a good benchmark as the results can be interpreted in the context of other models of new physics, and is useful for comparing the sensitivity of different experiments at the upgraded LHC. This work focuses on the study of the sensibility to these new particles in the HL-LHC. The first chapter will cover the SSM, while the second chapter will cover the study of the sensibility.

This work is part of an ATLAS note, which will be included in the next year's CERN Yellow Report, soon to be published. [6]

Chapter 1

Simulation of events with the Sequential Standard Model in ATLAS

While not usually the object of serious BSM searches, the Sequential Standard Model (SSM) is often used as a benchmark for search prospects, due to its simplicity, as well as historical reasons. In it, extra Z and W bosons are added, which have exactly the same couplings to fermions as the SM bosons. These new bosons are labeled Z′ and W′, and have higher masses than their SM counterparts. Many other theories or models predict similar particles (such as the E6, Left-Right Symmetric Models, and various GUT models, to name a few), and the SSM is used as the benchmark, as the results can be interpreted in the context of those other models (i.e. the results can give us an idea of how a Z' or W' would look in any of these theories).

With the upcoming High Luminosity Upgrade to the LHC, the final integrated luminosity is estimated to reach at least 3000 fb^{-1}. The ATLAS detector will undergo various upgrades to keep up with the increase in number of overlapping events, which are needed in order to collect the estimated integrated luminosity. This, in addition to the large increase of event statistics, will mean an improvement on the upper exclusion limits, or even a possible discovery of new particles. Thus, it prompts the development of search prospects, such as this one.

In this work, the prospects were made for a SSM Z′ search, with decays in the dileptonic channels, whereas for the SSM W′, the prospects are made for a search where the decay products are a lepton and a same flavored neutrino. Both of these prospects are only made in the electron and muon channels, since τ are not final state particles but decay mainly hadronically.

1.1 Data Simulation

Simulated Monte Carlo samples were produced considering an integrated luminosity of 3000 fb^{-1}, $\sqrt{s} = 14$ TeV, and 200 pileup interactions, which is expected at the HL-LHC.

1.1.1 Background

The main background, and the only one used for the Z' analysis, is the Drell-Yan (DY) production, which takes place when a quark of one hadron and an antiquark of another hadron annihilate, creating a virtual photon or Z boson which then decays into a pair of oppositely-charged leptons. For the W', the background comes from:

- $W^{\pm} \to \ell\nu$
- $t\bar{t} \to \ell\nu$
- di-boson $\to \ell\nu\,\ell\nu$
- di-boson $\to \ell\nu\,\nu\nu$

These backgrounds were selected given that they share the final state with the decays of this study, and are not negligible.

The DY, $W^{\pm} \to \ell\nu$, and $t\bar{t} \to \ell\nu$ backgrounds were generated using Powheg-Box [7], while the di-boson $\to \ell\nu\,\ell\nu$ and di-boson $\to \ell\nu\,\nu\nu$ backgrounds were generated using Sherpa [8].

1.1.2 Signals

The signals, on the other hand, are not produced directly, and instead a reweighting tool was used. The tool can generate signal templates for various BSM models from Leading

Order (LO) Pythia8 samples [9], thereby evading the issue of generating MC samples for each particular model and mass assumption of interest to an analysis. This is very useful, since we don't know the masses of the particles we want to study. For this reason, signal templates were generated for different SSM Z' and W' masses ranging from 3.5 TeV to 13.5 TeV, in increments of 1 TeV, assuming an integrated luminosity of 3000 fb^{-1} and $\sqrt{s}$ = 14 TeV.

1.1.3 Smearing

As previously mentioned, one of the main motivations of this work is to estimate the impact of the future detector upgrades, and in order to get an accurate estimation of the new limits, the truth data (i.e. generated data which assumes perfect conditions, too optimistic for a prospect) has to be smeared according to the expected detector capabilities.

A set of functions was produced using the detector layout described in the ATLAS Technical Design Reports [10–15], which are used to emulate the transverse energy and momentum resolutions, as well as efficiencies and fake rates of the different detectors. These functions were later applied to the data, which results in a much more realistic dataset. It should be noted though, since electrons and muons are the only relevant particles for this work, only those had their identification efficiency and resolution updated. Tests were done to see if the functions applied made sense, this can be seen in the broader peak of the muon channels, given their worse resolution at higher energies (figs. 2.1, 2.2). This occurs because muon observables are calculated from the tracks they leave on the Muon Spectrometer and Inner Detector, but at high energies the tracks become more and more like a straight line, and this makes their momentum difficult to resolve.

Chapter 2

Data Analysis

2.1 Event Selection

The event selections are similar to the ones used in the Run-2 analyses [16, 17]. These consider events that are consistent with the physics process which is to be measured. This helps in reducing some background sources, as well as selecting the data that fits the process more accurately. Aditionally, the same event selections are expected to be used in future analyses that will use real data.

2.1.1 Z' event selection

The selection criteria are as follows:

- Exactly two selected same-flavored leptons.
- At least one of those leptons must satisfy trigger conditions.
- Electrons:
  - $E_T > 25$ GeV
  - $|\eta| < 2.47$ (excluding $1.37 < |\eta| < 1.52$)
- Muons:
  - $p_T > 25$ GeV
  - $|\eta| < 2.65$

2.1.2 W' event selection

The selection criteria are as follows:

- One lepton must satisfy trigger conditions.
- Electrons:
  - $\mathrm{E}_T > 65$ GeV
  - $|\eta| < 2.47$ (excluding $1.37 < |\eta| < 1.52$)
  - MET > 65 GeV
- Muons:
  - $\mathrm{p}_T > 55$ GeV
  - $|\eta| < 2.5$
  - MET > 55 GeV

Where E_T is the energy of the particle measured along the plane transverse to the proton beam. p_T is the momentum of the particle along the same transverse plane. Finally, MET is the missing energy along the transverse plane.

2.2 Analysis and Results

2.2.1 Invariant Mass

A Z' boson signal would appear as an excess of events above the SM background at high dilepton invariant masses. The invariant mass is the total mass in the rest frame, and can be calculated in any inertial frame using the following formula:

$$M_{\ell\ell}^2 = m_1^2 + m_2^2 + 2\left(E_1\, E_2 - \vec{p_1}\cdot\vec{p_2}\right) \tag{2.1}$$

The invariant mass distributions for both decay channels are shown in figure 2.1. The differences in the shapes of the reconstructed Z' signals in the electron and muon channels arise from the effects of the object resolution.

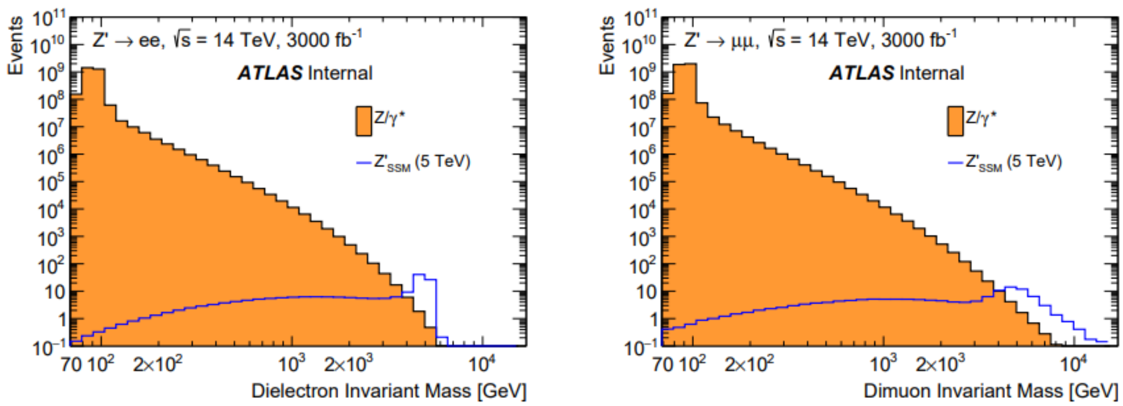

Figure 2.1: Invariant mass distributions for dielectron and dimuon channels, satisfying all selection criteria stated in section 7.1.1, and assuming an $\sqrt{s}$ = 14 TeV with an integrated luminosity of 3000 fb^{-1}. A 5 TeV SSM Z' signal was used as example [6].

2.2.2 Transverse Mass

For the W', on the other hand, since the final state includes a neutrino (which ATLAS can't detect directly), the invariant mass can't be used, since we can't measure its energy or momentum. Instead, the transverse mass is used, which for this case is defined as:

$$M_T^2 = m_\ell^2 + m_{\nu_\ell}^2 + 2\left(E_{T,\ell}\, E_{T,\nu_\ell} - \vec{p_{T,\ell}}\cdot\vec{p_{T,\nu_\ell}}\right) \tag{2.2}$$

The neutrino mass is taken to be 0 (a good approximation in this case), while p_{T,ν_ℓ} can be obtained by conservation of momentum. The distribution of M_T has an end-point at the invariant mass M of the system with $M_T \leq M$, which can be used to determine the mass of the original particle.

Now, the W' boson signal would appear as an excess of events above the SM background at high $\ell\nu$ transverse masses, examples of this are shown in figure 2.2. Once again, the differences in the shapes of the reconstructed W' signals in the electron and muon channels arise from the effects of the momentum resolution.

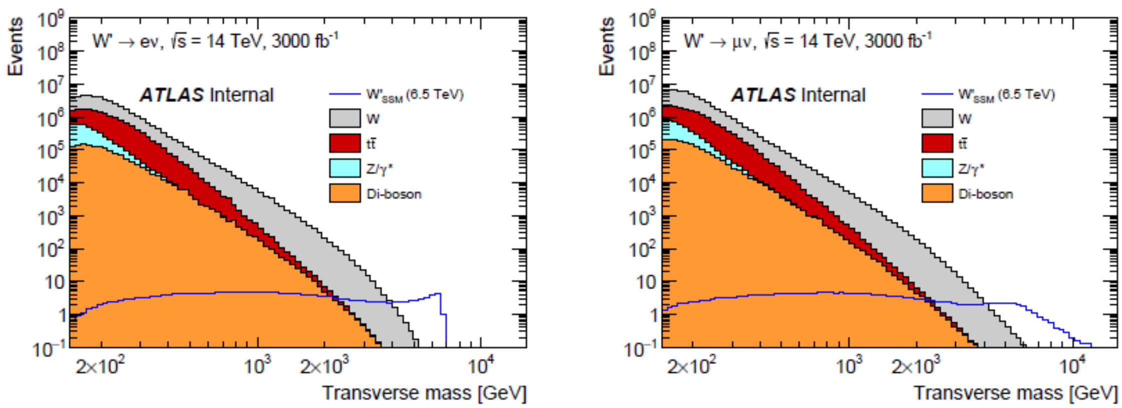

Figure 2.2: Transverse mass distributions for $e\nu$ and $\mu\nu$ channels, satisfying all selection criteria stated in section 7.1.2, and assuming an $\sqrt{s} = 14$ TeV with an integrated luminosity of 3000 fb^{-1}. A 6.5 TeV SSM W' signal was used as example [6].

2.2.3 Exclusion Limits and discovery reach

Asimov Datasets

A statistical analysis is performed for the searches for the Z' and W' bosons of the SMM, which uses Asimov datasets. The Asimov dataset is an artificial dataset created by setting the observed value in each bin exactly equal to the expectation value under some model hypothesis. The advantage of using such dataset comes from the reduced computation time needed to produce it, in comparison with the large number of pseudo-experiments used in a typical toy model.

2.2.4 Discovery Reach

Discovery limits are calculated in the asymptotic approximation given the large number of events from the LHC. A gaussian regime for the estimation is taken given the central limit theorem. The significance obtained from the likelihood ratio of the signal against the background-only hypothesis, is taken from counting events assuming a Gaussian or Poisson distributions. The former one is calculated as $\frac{s}{\sqrt{b}}$, or $\frac{s}{\sqrt{s+b}}$ in a more conservative way, while the latter is calculated as $\sqrt{2\big((s+b)\ln(1+s/b)-s\big)}$, which is also known as Asimov Significance. Given the small number of events, the correct test statistic would be the Asimov or the conservative Gaussian. For this example, various signal samples of a 5.5 TeV and a 6.5 TeV W' going to $e\nu$ were generated, assuming different integrated luminosities. The significances calculated then were:

1. Signal over the square root of the background: $\frac{s}{\sqrt{b}}$
2. Asimov Significance: $\sqrt{2\big((s+b)\ln(1+s/b)-s\big)}$
3. Signal over the square root of the signal plus the background: $\frac{s}{\sqrt{s+b}}$

Where the first case considers only the background uncertainties, and the third case considers both the signal and background uncertainties. The results of the comparison can be seen in figure 2.3.

For the 6.5 TeV signal, the result is only slightly affected by the significance definition used. However, for the 5.5 TeV W', about 10σ differences can be reached at a 3000 fb^{-1}, where the first significance calculation is the most optimistic, and the third is the most pessimistic, with the Asimov Significance landing right in the middle. For higher masses (with lower statistics), the method used has little impact on the final result. However, for signals with more statistics, the choice of which significance definition is used affects the final result. On the other hand, the higher mass significances cross the 5σ line at very different luminosities, whereas the low mass significances do it at similar values.

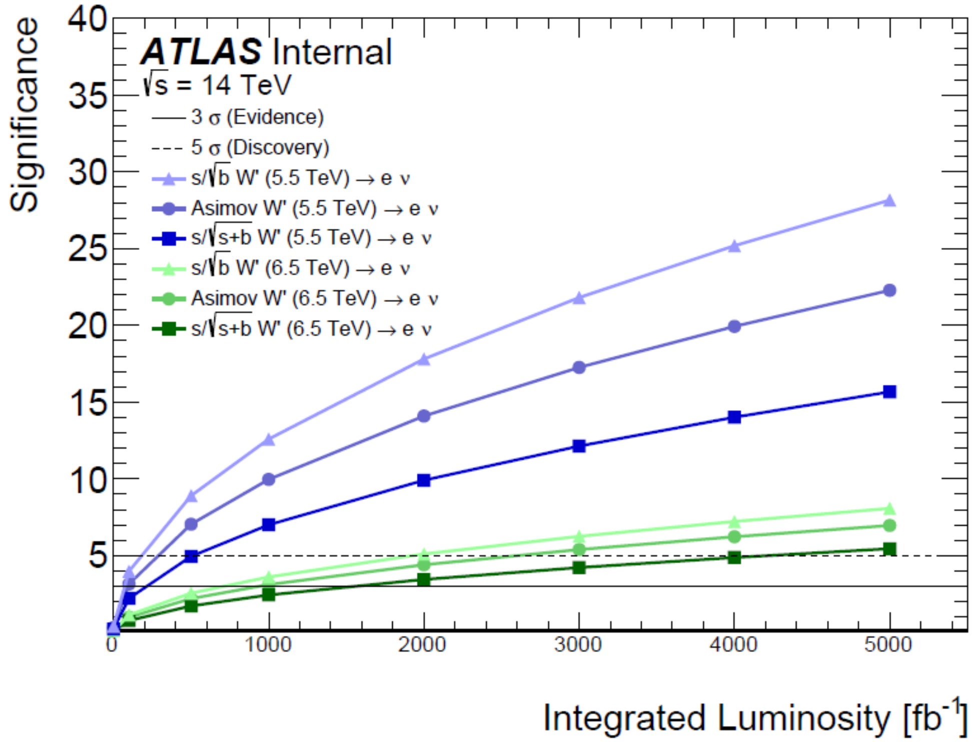

Figure 2.3: Significance Comparison for a 5.5 TeV and a 6.5 TeV SSM W' going to $e\nu$ [6].

With this information, the Asimov dataset was used for the Bayesian Analysis of the discovery reach.

Upper Limit

For the Z', the $M_{\ell\ell}$ distribution in the electron and muon channels is used as discriminant, whereas for the W' the discriminant used is the M_T distribution, also in the electron and muon channels. For the calculation of the exclusion limits the same methodology as in the Run 2 analyses is used, where the limits are calculated following Bayesian statistics [18]. The same statistical model implementation is used in the following for both the calculation of the exclusion limits and the discovery reach, the latter based on a profile likelihood ratio test assuming an asymptotic test statistic distribution [19].

The upper limits on the cross-section for producing a Z' (W') boson times its branching ratio to only one lepton generation ($\sigma\times$BR) are computed at the 95% CL as a function of the Z' (W') boson mass. The limits are calculated with a uniform positive prior probability distribution for $\sigma\times$BR. The observed upper limits are extracted by comparing data to the expected background and signal using SSM Z' (W') templates which are binned in $M_{\ell\ell}$ (M_T for W'), with masses in the search range 3.5 TeV $\leq M_{Z'} \leq$ 11.5 TeV. The expected limits are derived from Asimov pseudo-experiments obtained from the estimated background distributions. The median of the distribution of the limits from the pseudo-experiments is taken as the expected limit, and 1σ and 2σ bands are defined as the ranges containing respectively 68% and 95% of the limits obtained with the pseudo-experiments. The results of the statistical analysis for the SSM bosons' exclusion limits are visualized in figure 2.4.

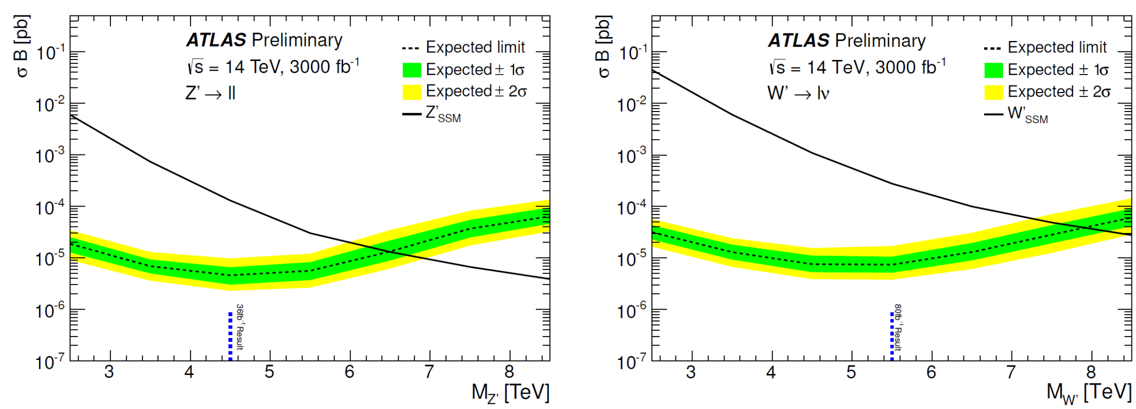

Figure 2.4: The left plot (right plot) shows the expected upper limits (dashed line) on the $\sigma\times$BR of the SM background, as a function of the hypothetic Z'_{SSM} boson mass (W'_{SSM} boson mass), in the combined electron and muon channels. The 1σ (green) and 2σ (yellow) expected limit bands are also shown. The predicted $\sigma\times$ BR for SSM Z' (W') production is shown as a black line. The blue markers show the current limits obtained with the latest Run 2 analysis based on 79.8 fb^{-1} of data. Plots assume an integrated luminosity value of 3000 fb^{-1} and a centre of mass energy of 14 TeV [6].

The production of SSM bosons is very high for the lower hypothetical masses of the bosons. This is reflected on the plot, where the black line is above the expected SM background production. The place where the expected signal and background distributions (black and dashed lines) cross, shows the upper exclusion limit: in case no particle is observed, then SSM bosons up to this mass can be excluded. It is not possible to produce the SSM bosons when the signal (black line) crosses below the expected background.

As mentioned at the beginning of this section, the same statistical model implementation is used for the discovery reach calculation. The results of the full statistical analysis are summarized in table 2.1.

Decay	Exclusion [TeV]	Discovery [TeV]
$Z' \to ee$	6.4	6.3
$Z' \to \mu\mu$	5.8	5.7
$Z' \to \ell\ell$	6.5	6.4
$W' \to e\nu$	7.6	7.5
$W' \to \mu\nu$	7.3	7.1
$W' \to \ell\nu$	7.9	7.7

Table 2.1: Exclusion Limits and Discovery Reach on the electron, muon and combined decay channels for both Z' and W'.

For both cases, this is an improvement of more than 2 TeV with respect to the current exclusion limits using 79.8 fb^{-1} of $\sqrt{s} = 13$ TeV of data. One can also see, that in both cases the limits in the electron channel are higher that on the muon channel, this is due to the calorimeter resolution, which is much better than the muon spectrometer one for very high-p_T leptons.

Conclusion

The first part of this work summarizes the cosmic ray tests performed for the sTGC modules of the ATLAS NSW. The ATLAS detector at the LHC, CERN, will undergo upgrades after the latests data taking period: Run 2. One of these upgrades is the New Small Wheel, which will change the endcap muon spectrometer. This upgrade is required, since at the time most of the hits in that part of the detector are fake, due to the lack of tracking capabilities of the current Small Wheels. The NSW will solve this problem, and will also improve the momentum resolution. In addition, its faster trigger rate will allow the endcap muon spectrometer to keep functioning even during the last stage of the LHC, the High Luminosity LHC, which will have an extremely large rate of events (which the current SW would not be able to cope with). The NSW will be comprised of two detector technologies, the MicroMegas and the small-strip Thin Gap Chambers. The sTGCs are being build in 5 countries, one if these being Chile, in a joint collaboration between the PUC and the UTFSM. In this work, details about the sTGC construction are outlined, while assembly of the electronics is explained more carefully. Pad and Strip Adapter Boards are soldered to the sides of the detector, while Wires Adapter Boards are attached to the ends. After construction is finished, cosmic ray tests must be perfomed on the detectors. For these tests, Front End Boards are attached temporarily to the Adapter Boards, later to be removed before shipping the detector to CERN.

The cosmic ray tests are described in further detail. First, a trigger system, which uses an FPGA and arrays of plastic scintillators is presented. This trigger system checks for coincidences between an array placed on top of the detector, and one placed below it. When a coincidence is detected, a trigger signal is sent to the data aquisition system. This DAQ system, consists of the FEBs attached to the detector, an FPGA, and a PC to control the whole system. The PC uses custom software to communicate with the FEBs, send configurations, set detection thresholds, mask unwanted channels, among other things. When a muon crosses the setup, a trigger signal is sent to the DAQ, which takes the data from the detector, processes it, and saves it in the PC as a binary file to later be analyzed. The results show information about the efficiency of the detector, which is needed for Quality Assurance reasons, as specified in the New Small Wheel Technical Design Report.

The setup has been used succesfully to test one QS1 module, which has been shipped to CERN and integrated into the first production wedge. In the future, the setup will continue to be used and optimized, to ensure that the Chilean modules satisfy the quality expectations of the ATLAS collaboration.

The second part summarises the prospects for searches for new heavy SMM Z' and W' bosons at the HL-LHC, which is expected to run at $\sqrt{s} = 14$ TeV and collect 3000 fb^{-1} of data. These studies are based on MC simulations. To simulate the response of the upgraded ATLAS detector and pile-up collisions the MC truth information is convoluted with parameterised estimates to emulate the response of the upgraded ATLAS detector and pile-up collisions. SSM Z' bosons are searched for in the dilepton final states, and could be discovered at the HL-LHC up to a mass of 6.4 TeV. In case no signs for such particle are found, it can be excluded up to SSM Z' mass of 6.5 TeV. Another search uses the SSM W' boson as benchmark and studies the lepton plus neutrino final state. The lower exclusion limit at 95% CL on the SSM W' pole mass is expected to improve from 5.6 TeV currently to 7.9 TeV. If such a particle exists it can be discovered up to a SSM W' mass of 7.7 TeV.

Bibliography

[1] ATLAS Collaboration, *Observation of a new particle in the search for the Standard Model Higgs boson with the ATLAS detector at the LHC*, Submitted to Phys. Lett. B (2012), arXiv:1207.7214 [hep-ex]

[2] Drawn by Arpad Horvath; adapted by User Jaybear, *The LHC experiments and the preaccelerators,* Wikimedia Commons.

[3] ATLAS Collaboration, *The ATLAS Experiment at the CERN Large Hadron Collider,* JINST 3 (2008) S08003.

[4] ATLAS Magnet System Diagram, `http://www.quantumdiaries.org/wp-content/uploads/2011/05/exp-magnets.png`

[5] Kawamoto, T; Vlachos, S; Pontecorvo, L; Dubbert, J; Mikenberg, G; Iengo, P; Dallapiccola, C; Amelung, C; Levinson, L; Richter, R; Lellouch, D; *New Small Wheel Technical Design Report,* CERN-LHCC-2013-006, ATLAS-TDR-020, June 2013, `https://cds.cern.ch/record/1552862`

[6] Donini, Julien and Duncan, Anna Kathryn and Hayden, Daniel and Kubota, Shion and Lee, Graham Richard and Marjanovic, Marija and Ochoa, Jean-pierre and Rivera Vergara, Juan Cristobal and Wielers, Monika and Willocq, Stephane and Bugge, Magnar Kopangen and Lin, Kuan-yu and Vaslin, Louis, *Prospects for searches for heavy Z' and W' bosons with the ATLAS experiment at the HL-LHC*, ATL-COM-PHYS-2018-414, `https://cds.cern.ch/record/2314394`

[7] S. Alioli, P. Nason, C. Oleari, and E. Re, *A general framework for implementing NLO calculations in shower Monte Carlo programs: the POWHEG BOX*, JHEP 06 (2010) 043, arXiv: 1002.2581 [hep-ex]

[8] T. Gleisberg et al., *Event generation with SHERPA 1.1*, JHEP 0902 (2009) 007, arXiv: 0811.4622 [hep-ph].

[9] T. Sjöstrand, S. Mrenna, and P. Z. Skands, *A brief introduction to PYTHIA 8.1*, Comput. Phys. Commun. 178 (2008), arXiv: 0710.3820 [hep-ph]

[10] ATLAS Collaboration, *Technical Design Report for the Phase-II Upgrade of the ATLAS Muon Spectrometer*, CERN-LHCC-2017-017. ATLAS-TDR-026, 2017, url: `http://cds.cern.ch/record/2285580`

[11] ATLAS Collaboration, *Technical Design Report for the ATLAS LAr Calorimeter Phase-II Upgrade*, CERN-LHCC-2017-018. ATLAS-TDR-027, 2017, url: `http://cds.cern.ch/record/2285582`

[12] ATLAS Collaboration, *Technical Design Report for the ATLAS Inner Tracker Strip Detector*, CERN-LHCC-2017-005. ATLAS-TDR-025, 2017, url: `http://cds.cern.ch/record/2257755`

[13] ATLAS Collaboration, *Technical Design Report for the Phase-II Upgrade of the ATLAS Tile Calorimeter*, CERN-LHCC-2017-019. ATLAS-TDR-028, 2017, url: `http://cds.cern.ch/record/2285583`

[14] ATLAS Collaboration, *Technical Design Report for the Phase-II Upgrade of the ATLAS TDAQ System*, CERN-LHCC-2017-020. ATLAS-TDR-029, 2017, url: `http://cds.cern.ch/record/2285584`

[15] ATLAS Collaboration, *Technical Design Report for the ATLAS Inner Tracker Pixel Detector*, CERN-LHCC-2017-021. ATLAS-TDR-030, 2017, url: `http://cds.cern.ch/record/2285585`

[16] ATLAS Collaboration, *Studies of Sensitivity to New Dilepton and Ditop Resonances with an Upgraded ATLAS Detector at a High-Luminosity LHC*, ATL-PHYS-PUB-2013-003, 2013, url: `http://cds.cern.ch/record/1516108`

[17] ATLAS Collaboration, *Search for a new heavy gauge boson resonance decaying into a lepton and missing transverse momentum in 79.8 fb-1 of pp collisions at $\sqrt{s}$ = 13 TeV with the ATLAS experiment*, ATLAS-CONF-2018-017, 2018, url: `https://atlas.web.cern.ch/Atlas/GROUPS/PHYSICS/CONFNOTES/ATLAS-CONF-2018-017/`

[18] A. Caldwell, D. Kollar, and K. Kroninger, *BAT: The Bayesian analysis toolkit*, Comput. Phys. Commun. 180 (2009) 2197, arXiv: 0808.2552 [physics.data-an]

[19] G. Cowan, K. Cranmer, E. Gross, and O. Vitells, *Asymptotic formulae for likelihood-based tests of new physics*, Eur. Phys. J. C 71 (2011) 1554, [Erratum: Eur. Phys. J.C73,2501(2013)], arXiv: 1007.1727 [physics.data-an]